A hit correlation approach to the KM3NeT detector calibration

van Loon, Björn

A hit correlation approach to the KM3NeT detector calibration

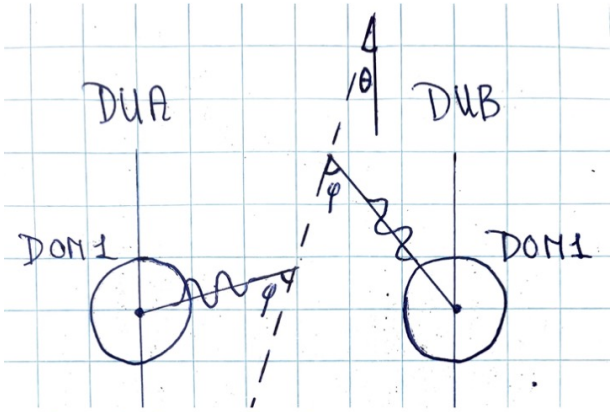

Back to the drawing board...

THESIS

submitted in partial fulfillment of the
requirements for the degree of

BACHELOR OF SCIENCE
in
PHYSICS

Author :	B.F.J.W. van Loon
Student ID :	2524406
Supervisor :	D.F.E. Samtleben
Second corrector :	T.H. Oosterkamp

Leiden, The Netherlands, June 30, 2023

A hit correlation approach to the KM3NeT detector calibration

B.F.J.W. van Loon

Huygens-Kamerlingh Onnes Laboratory, Leiden University
P.O. Box 9500, 2300 RA Leiden, The Netherlands

June 30, 2023

Abstract

KM3NeT is a collaboration that is currently constructing a research infrastructure in the Mediterranean Sea, consisting of deep-sea neutrino telescopes. Its main scientific goals are to probe into the cosmos for high-energy neutrino sources, and to determine fundamental properties of these particles. These goals are pursued by dividing the detector volume over two sites, ORCA and ARCA, each housing a detector that is optimised for a distinct energy range. To achieve the final science, KM3NeT requires a time and position calibration accuracy of roughly 1 ns and 20 cm, respectively. This study presents an examination of two independent calibration methods, which utilise the detection of muons produced by cosmic ray showers. The time calibration provides consistent results for different cuts of data. When the movement of detection units due to varying sea currents is low, the systematic error is entirely explained via an asymmetry in the detector geometry. Ultimately, an accuracy of 2.5 ns is achievable. The position calibration is a novel technique that is developed during this project. We demonstrate its feasibility by applying it to the detector data, and estimate the currently obtainable accuracy to be within 2 m. Although both methods currently cannot meet the standards set by KM3NeT, their techniques are far from perfected. Overall, a fast cross check of the existing calibration techniques can be provided, while requiring no additional setups or measurements.

Contents

Chapter 1

Introduction

The first chapter of this paper addresses the purpose of this study within the larger scope of research objectives set by the KM3NeT group. The initial sections will provide an introduction to their research infrastructure and how it is exploited to achieve the scientific goals. During this process, a signal produced by atmospheric muons is encountered, which is typically disregarded in the study of neutrinos but forms the very foundation of this study. We will dedicate two sections to the origin and properties of these particles, to display their suitability for the methods presented in this paper. The aim of this study is to provide robust methods, capable of both time and position calibration of detection units, that may be used as complementary to existing techniques.

1.1 KM3NeT

This research project is carried out in collaboration with the KM3NeT group of Nikhef, based in Amsterdam. Scientists of KM3NeT have formed a collaboration to build and operate a new research infrastructure, which consists of a network of deep-sea neutrino telescopes in the Mediterranean Sea [1]. When finalised, the construction will have a detector volume of roughly a cubic kilometre of seawater, which gives birth to the group its name (**km**^{3} **Ne**utrino **T**elescope). This volume is divided over two deep-sea sites, that is off-shore Toulon (France) and Capo Passero (Sicily, Italy) [1][1]. Each of these sites contains the so-called building blocks of the infrastructure: 3-dimensional arrays of optical sensors which are used to detect Cherenkov light induced by charged particles propagating through

[1] In the far future, one may be realised in Pylos (Peloponnese, Greece) as well.

Version of June 30, 2023– Created June 30, 2023 - 14:00

the seawater. These building blocks will consist of 115 vertical Detection Units (DUs) or otherwise referred to as 'strings', composed of 18 Digital Optical Modules (DOMs). An individual DOM contains 31 photomultiplier tubes (PMTs) which are distributed almost isotropically [2]. A more in-depth description of the research infrastructure is found in a letter of intent written by the KM3NeT collaboration [1]. At the time of writing, two building blocks have been realised partially: these are referred to as KM3NeT/ARCA or ARCA (Astroparticle Research with Cosmics in the Abyss) and KM3NeT/ORCA or ORCA (Oscillation Research with Cosmics in the Abyss). Both are optimised for different energy ranges and, as their name suggests, serve a different purpose in the study of neutrinos.

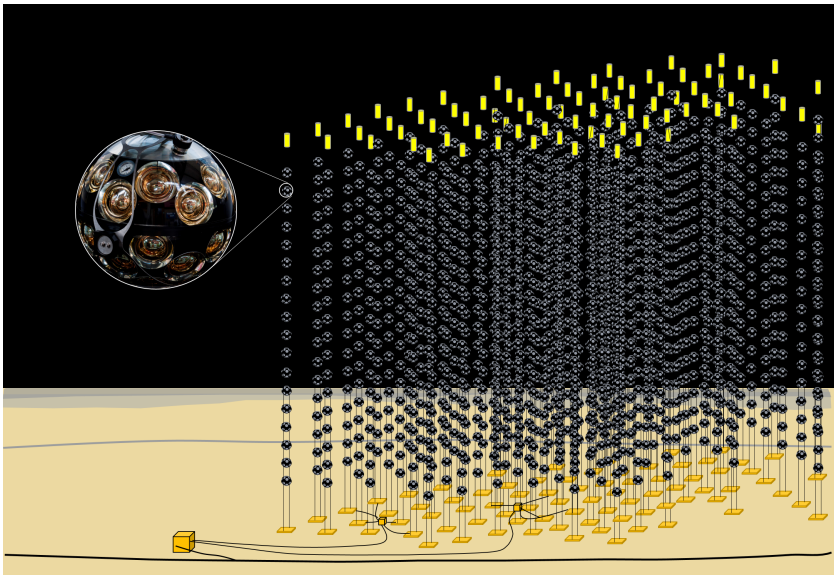

Figure 1.1: *An artist's impression of the string network. To keep their alignment as vertically as possible, the DUs are kept under tension by attaching it to the bottom of the ocean with a base, and introducing a buoy at the top. The upper left displays a photograph of one of the DOMs. Adapted from* `https://www.km3net.org/`.

1.2 KM3NeT/ARCA

Located about 100 km offshore from Portopalo di Capo Passero, Sicily, ARCA features DUs of about 700 metres in length, with an average horizontal spacing of ∼90 metres. Along the vertical direction of the DUs, DOMs are spaced 36 metres apart, starting at 80 metres from the sea floor.

This design optimises ARCA in the TeV-PeV range, which makes it ideal for detecting high-energy cosmic neutrinos. Evidence for these particles was initially presented by the IceCube Neutrino Observatory in 2013 with high significance [3]. This discovery served as a major landmark in the history of neutrino astronomy [1], as their energetics imply the existence of powerful cosmic particle accelerators. Although the origin of these neutrinos remains unknown, the search for possible sources continues. The first stand-alone detected neutrino source is thought to be galaxy NGC 1068, also known as Messier 77. A study of the IceCube collaboration in 2022 has provided evidence of high-energy neutrino emission from its Active Galactic Nucleus (AGN) [4]. Galaxies that contain an AGN have long been considered as potential neutrino emitters, as they place among the most energetic astrophysical objects in the cosmos. Other promising candidate sources are Gamma-Ray Bursts (GRBs): short and powerful flashes of electromagnetic radiation, releasing 10^{51} to 10^{54} ergs in just a few seconds [5]. Even within our own galaxy, several objects have been proposed to be neutrino production sites, with Supernova Remnants (SNRs) being the most compelling candidates. As its geographical location allows for an almost complete observation of the Galactic Plane, one of ARCA its primary goals is the detection of these Galactic sources. This brings us to one of its advantages: namely its ability to observe in the 10 TeV range, in which the IceCube ability to detect muon neutrinos is limited [6].

Currently, 21 DUs have been installed. When realised in its entirety, i.e. both of its building blocks have been fully constructed, ARCA will have a wider and complementary field of view, surpassing that of the IceCube detector. In addition to its main objective to probe into high-energy neutrino sources, ARCA will also aid in the study of other aspects of physics such as dark matter, violation of Lorentz invariance (LIV), exotic particles and multi-messenger astronomy [1].

1.3 KM3NeT/ORCA

Although similar in construction to ARCA, ORCA has an average horizontal spacing of $\sim$20 metres between its 200 metre long DUs, with DOMs distributed about 9 metres apart from each other. It is situated 40 km offshore from Toulon, starting about 40 metres from the bottom of the sea, and is specialised in the detection of neutrinos in the GeV energy range. Hence, the primary goal of ORCA is to determine the neutrino mass hierarchy (NMH) [1]. Our current understanding of neutrinos considers three known flavour eigenstates: ν_e, ν_μ, ν_τ (electron, muon and tau neutrinos).

These flavours are superpositions of three mass eigenstates (ν_1, ν_2, ν_3) with corresponding masses (m_1, m_2, m_3). While the existence of these masses has been determined, their ordering has not. Furthermore, the mixing of flavour eigenstates is characterised by a set of four parameters. While the available data have provided insight, ambiguity about some of their values still remains [7]. On their current course, next-generation accelerator experiments like DUNE and T2HK are set to solve the NMH by 2030 at its earliest. Therefore, alternative methods like the ORCA and JUNO (Jiangmen Underground Neutrino Observatory) detector are being considered, as they plan to unravel the ordering of masses within a shorter time span. Finding the NMH may also have a strong impact on the performances of future experiments that measure other fundamental properties of neutrinos, such as their absolute masses, potential Majorana nature (i.e. being their own antiparticle) and whether CP-violation occurs in the neutrino sector [8]. Additionally, ORCA might delve even further into possible extensions of the standard model. Recent experiments have reported results which are inconsistent with the current three neutrino framework. Such anomalies can be eliminated by introducing a fourth neutrino that has low mass and cannot participate in weak interactions. The latter property is what grants it its name: the *sterile neutrino*. By making use of atmospheric neutrinos, next-generation detectors like ORCA are able to test this hypothesis [9].

Just like its Italy-sited counterpart, ORCA is still under construction: when finalised, it will host one building block. As of now, 18 DUs have been deployed, with 16 of them being operational.

1.4 Detection

Research conducted by KM3NeT relies on the detection of neutrinos: this, however, is easier said than done. Their light mass and neutral charge makes them (nearly) impervious to gravitational and electromagnetic interactions. As a result, the only interactions they undergo are via the weak force. Detection of neutrinos hence happens indirectly via Cherenkov radiation generated by relativistic particles that arise from these weak interactions [1]. We identify two distinct phenomena that may occur: shower- and track-like events.

Shower- or cascade-like events are produced by the matter near or inside the detector. It can either be caused by a charged-current (CC) in-

teraction of an electron (anti)neutrino or a neutral-current (NC)[2] interaction of all (anti)neutrino flavours. The result is an electron/positron and some hadronic composition which respectively cause an electromagnetic and hadronic shower (in the NC case, only a hadronic shower is generated). Electromagnetic cascades are driven by the emission of photons via bremsstrahlung[3], which again produces electron-positron pairs via pair production. Hadronic cascades evolve in a similar manner, but are dominated by the decay of particles. Their structure may also be more complex, containing both hadronic and electromagnetic showers [1].

Track-like events are the result of muons produced in the matter inside or surrounding the detector via the CC interactions of muon (anti)neutrinos. While cascades are confined to a relatively small space, tracks can span much greater distances, with muons at energies above 1 TeV reaching track lengths of the order of kilometres. Note that CC interactions of tau neutrinos have not yet been mentioned: these have a 83% probability of causing cascades, while the remaining 17% produces track-like events resulting from the tau particle decaying into a muon [1].

Both signatures have something in common: they are detected via a phenomenon known as Cherenkov radiation. When a charged particle propagates through matter, it polarises the atoms in the medium. If the particles velocity v is larger than the phase velocity of light c/n, where n denotes the refractive index, the environment atoms emit radiation along a narrow cone that has its axis aligned with the particle's trajectory. The direction of emission is characterised by apical angle θ_c, defined as $\cos\theta_c = c/(vn)$ [10]. Projecting a two-dimensional plane perpendicular to the particle's trajectory results in characteristic ring patterns known as Cherenkov rings, which are detected by the PMTs. These definite rings can only be observed for track-like events: due to the shower structure, not all particles propagate along the shower axis. Additionally, bremsstrahlung is generated as these particles are deflected by the seawater nuclei. The emitted photon will typically create an electron-positron pair, which is able to produce more bremsstrahlung. As a result, an emission spectrum is measured along the shower axis. The bulk, however, can still be found around the Cherenkov angle [11].

[2]Charged/neutral-current interactions are weak interactions that result from the exchange of a (charged) $W^{\pm}$ and (neutral) Z^0 boson.

[3]Photons produced by the deceleration of charged particles, in this case caused by nucleii in the sea-water or detector.

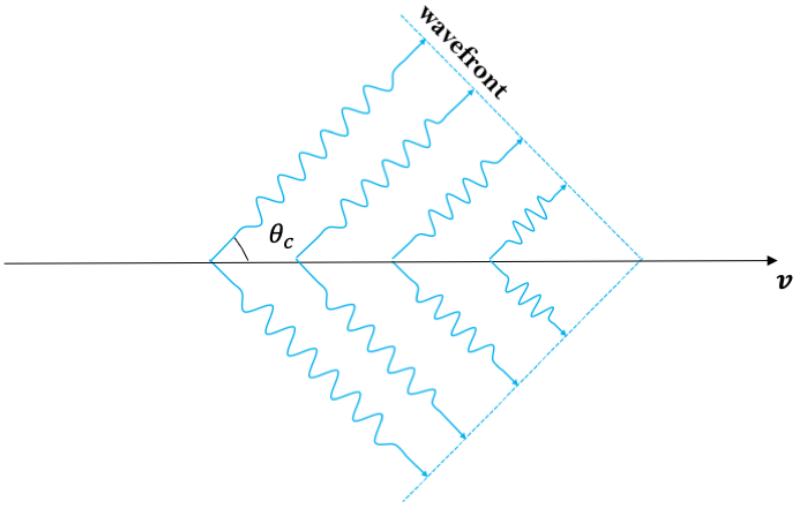

Figure 1.2: *A 2D illustration of the Cherenkov wave geometry. The size of the ring patterns observed are dependent on angle θ_c, and therefore directly related to the particle velocity v (which is assumed to be uniform) and refractive index n.*

1.5 Data acquisition

When the signal on a PMT is sufficient, the threshold is passed (which is set to 0.3 photo-electrons) and a hit is registered. This is commonly referred to as an L0 hit, as in this stage a 'level-zero' filter has been applied to the data. The L0 hit contains three pieces of information: the PMT address, time and time over threshold, i.e. the total duration threshold has been reached. Once the data are on shore, additional filters can be applied. A level-one or L1 hit requires at least two L0 hits from different PMTs in the same DOM, within a time frame that is typically set to 10 ns. Every 100th found L1 hit is stored. Within these hits, another selection is made and stored: this considers coincidence of at least 4 PMTs, also referred to as *supernova (SN) hits*[4]. When a coincidence of SN hits is identified to be from the same source, a *hit correlation* is registered. Additionally, data are saved when correlations of hits between at least 5 DOMs were identified within a time period of a few microseconds. These *events* are consistent with either a track or shower signature. The final filter that is utilised is a high rate veto (HRV): when the hit rate of a single PMT exceeds 20 kHz, the data recorded is excluded from going to shore. When combined, these filters increase the signal-to-noise ratio as background signals have a higher

[4] A supernova signal, which consists of many low energy neutrinos, would manifest itself in an enhanced correlated rate measured at all DOMs.

chance of being excluded [1]. The resulting (mostly continuous) stream of data is divided into *runs*; these periods may last a few minutes up to several hours.

1.6 Optical background

Aside from the Cherenkov radiation generated by neutrino interactions, the PMTs may register L0 hits triggered by other optical background sources. The first and foremost cause is the radioactive decay of potassium-40, which naturally occurs in sea salt. In most cases ($\sim 89\%$) it decays into calcium-40 via beta decay[5]:

$$^{40}\mathrm{K} \rightarrow {}^{40}\mathrm{Ca} + e^{-} + \bar{\nu}_e \tag{1.1}$$

The electron is able to induce Cherenkov radiation, provided its velocity is sufficient[6]. Noise caused by this process can be greatly reduced by applying the L1 hit. If multiple L0 were to be registered on the same DOM, the ^{40}K decay data can be used to calibrate its PMTs [12]. Light may also be produced by living organisms: this *bioluminescence* causes a sudden increase in hit rates on a single DOM for possibly a few seconds. As this signal serves no purpose, the HRV is introduced to the data.

The final source plays a vital role in this project. Before delving into this subject, a brief introduction regarding its origin would be appropriate.

1.7 Cosmic rays

As their name implies, cosmic rays are high-energy charged particles that originate from outer space. While composed of several particles such as electrons, atomic nuclei and antiparticles, the main contributors to the observed flux are protons[7]. Once arrived at the upper layer of Earth's atmosphere, these rays interact, producing a cascade of secondary particles which is also referred to as a *cosmic ray air shower*. We distinguish two types of interactions that may occur.

[5] The remainder mostly decays into ^{40}Ar via electron capture, emitting a neutrino and gamma ray.

[6] About 21% produces electrons with sufficient energy [11].

[7] Although recent studies have shown that the highest energy cosmic rays are primarily heavier nuclei [11].

Version of June 30, 2023– Created June 30, 2023 - 14:00

Hadronuclear interactions are caused by the interactions of protons with the surrounding matter. The most predominant ones are

$$p + p \rightarrow \begin{cases} p + n + \pi^+ \\ p + p + \pi^0 \end{cases} \tag{1.2}$$

and

$$p + n \rightarrow \begin{cases} p + n + \pi^0 \\ p + p + \pi^- \end{cases} \tag{1.3}$$

which are expected to produce equal amounts of charged (π^+, π^-) and neutral (π^0) pions. Another type of reaction that falls under this category is the production of *mesons*: particles comprising a quark-antiquark pair[8]. While a large range of configurations is possible, creating all sorts of exotic mesons, most of them are short-lived, quickly decaying into one of their lightest components: $K^\pm$ and K^0 mesons or kaons. Kaons have a relatively short mean lifetime as well (order 10^{-8} s at most) and decay into either (anti)muons or pions ($\pi^\pm$ or π^0) [13].

Alternatively, cosmic rays may undergo *photohadronic interactions* with photons in the atmosphere. This produces a (virtual) Δ^+ particle[9], which generates positively and neutrally charged pions via its two main decay channels

$$p + \gamma \rightarrow \Delta^+ \rightarrow \begin{cases} p + \pi^0 \\ n + \pi^+ \end{cases} \tag{1.4}$$

that respectively have a 67% and 33% probability of being realised [11]. The last process is what gives rise to the largest contributor to optical background flux; namely the decay of charged pions into (anti):

$$\begin{aligned} \pi^\pm &\rightarrow \mu^\pm + \overset{(-)}{\nu}_\mu \\ \pi^0 &\rightarrow \gamma + \gamma \end{aligned} \tag{1.5}$$

Where $\overset{(-)}{\nu}_\mu$ denotes a muon (anti)neutrino. This happens relatively fast as well, as the mean lifetime of pions is of the same order as kaons. Photons resulting from the neutral pion decay are able to produce electron-positron (e^+e^-) pairs, which, as mentioned in Section 1.4, cause electromagnetic cascades. The (anti) muons produced through the decay channels of kaons and charged pions are more commonly referred to as *atmospheric muons*.

[8] An example of these would be the pions just mentioned.

[9] A baryon that has the same quark composition as a proton (uud), with slightly heavier mass.

1.8 Atmospheric muons

The cosmic ray air shower may consist of a complex network of several secondary particles. Yet at ground level, mostly (anti) muons are detected. This section will discuss what causes this limited detection of all other particles produced by cosmic rays.

Charged particles in the cosmic air shower lose energy via both ionisation of the surrounding matter and radiative processes, with the main contributors being bremsstrahlung and e^+e^- pair production. A critical energy E_c is introduced, which defines two regimes. For particle energies $E < E_c$, interactions that cause ionisation become the main cause of the energy loss, while for higher energies $E > E_c$ the radiative processes dominate. For both muons and electrons/positrons, ionisation losses are similar, being approximately 2 GeV once at sea level. However, the power irradiated by bremsstrahlung is dependent on the Lorentz factor $\gamma = E/mc^2$ with at least γ^4, which suppresses radiation losses for muons significantly as $m_\mu/m_e \sim 200$. As a result, electrons/positrons and muons have critical energies $E_{c,e} \sim 80$ MeV and $E_{c,\mu} \sim 3$ TeV, respectively [14]. The majority of muon flux resides in the < 100 GeV range due to the decay behaviour of pions (as will become clear shortly). For energies E_μ below $\sim$1 GeV, muon decay and energy loss take over, which prohibit them from reaching the surface of the Earth. At higher E_μ (10-100 GeV), the particles retain enough energy to propagate to the detector before decaying. For example, a muon with $E_\mu \sim 10$ GeV corresponds to $\gamma \sim 100$. The distance traveled by a highly relativistic unstable particle, also known as the *mean decay length*, is roughly given by $l_d = \gamma\tau c$, where τ is the mean lifetime in its rest frame. As, $\tau_\mu \sim 2\,\mu$s, muons are able to cross a distance of at least 60 km, which is more than enough to reach the detector[10]. Contrarily, electrons/positrons generated in electromagnetic cascades quickly dissipate their energy via radiative processes, and once below E_c lose the rest via ionisation, well before reaching sea level.

For pions, a similar reasoning follows. Having a mass similar to muons, but a mean lifetime of roughly two orders of magnitude lower, charged pions ($\pi^\pm$) are much more prone to decay as $l_{d,\mu}/l_{d,\pi} \sim 100$ for equal energetics. At higher energies above the threshold $E_{c,\pi} \sim 100$ GeV, $\pi^\pm$ rapidly lose their energy via interactions with air nuclei, producing new charged pions with a typical multiplicity of 20 [14]. Once their energy exceeds below $E_{c,\pi}$, $\pi^\pm$ are more likely to decay than interact, as the decay length (which is roughly 600 metres at most) surpasses the interac-

[10] Muons are typically produced high in the atmosphere, at a height of 15km [15].

Version of June 30, 2023– Created June 30, 2023 - 14:00

tion length[11]. An analogous statement can be made about kaons: while their lifetime is (at most) roughly the same as charged pions, the mass ratio $m_K/m_\mu \sim 3.5$, which corresponds to an even shorter decay length. Neutrally charged pions (π^0) have $\tau \sim 10^{-17}$ s, and therefore almost instantaneously decay into two photons [14].

Finally, we arrive at protons and neutrons, jointly called *nucleons*. These clearly need another explanation, as their mass is sufficiently high ($m_{p,n}/m_\mu \sim 9$) and their lifetime[12] would allow them to easily reach the detector. The answer lies within their constituents: unlike the muon, which is a lepton, nucleons are composed of quarks. These particles carry so-called 'colour charge' which allows them to act via the strong nuclear force, in addition to the gravitational, weak and electromagnetic interactions leptons experience as well. Consequently, protons and neutrons are more likely to interact throughout their course towards Earth, limiting their ability to reach the surface.

Atmospheric muons have a great resemblance of track-like events, with a signal rate several orders of magnitude higher than that of neutrinos. Hence, for the final science of KM3NeT, this background has to be removed from the data in order to prevent false identification of neutrino events. This is achieved by only selecting events that move upward, as (anti) muons are unable to traverse the Earth [11]. However, the high signal rate and ability to travel large distances are precisely what makes this research viable, as the required data can be gathered relatively fast. This gives rise to one of the advantages of the methods covered in this paper, which we will further elaborate on in Section 1.10.

1.9 Calibration

Ultimately, KM3NeT uses the acquired data to make reconstructions of the neutrino events in order to determine the parameters of interest, that is, their energy and direction. This is accomplished by using maximum likelihood (ML) methods tailored to each type of event. For optimal results, these techniques require the DOMs to be synchronised with nanosecond accuracy, and their position to be known within $\sim$ 20 cm[13]. To achieve these goals, KM3NeT uses a couple of methods: this section will focus on the ones that are currently in use.

[11] That is, the mean distance travelled before undergoing an interaction.
[12] About 15 minutes for neutrons and presumably infinite for protons.
[13] Light travels roughly 1 metre per 5 nanoseconds in seawater.

Time calibration consists of three steps: determining relative time offsets between PMTs within a DOM (intra-DOM), DOMs on a DU (inter-DOM) and DUs (inter-DU). As previously mentioned, the Cherenkov light produced by ^{40}K decay is utilised to perform intra-DOM time calibration. The produced electrons retain sufficient energy for a few centimetres on average, such that a couple of PMTs register a hit. As there is not only a natural abundance of ^{40}K in the seawater, but in the glass sphere of a DOM as well, this method can be applied before deployment and *in situ* (i.e. after the deployment of the DUs) [16]. As of now, inter-DOM calibration solely relies on a method that is performed pre-deployment. It considers a blue laser that illuminates 1 PMT on all DOMs simultaneously using a splitter. When relative time offsets between DOMs are introduced, the PMTs measure the laser at different instances. These time differences between detection events can be used to correct all modules relative to a reference DOM. As far as in situ methods concerned, there are currently 2 in development. The first utilises LED beacons that are located in the top half of each DOM by sending short pulses that can be measured at multiple modules. Expected and measured arrival time of light can be compared to determine the relative offsets between DOMs. The second method involves a similar analysis, but now hit times are predicted by reconstructing muon trajectories. Both techniques require the DOM positions to be known: it is only recently that we have been able to achieve this using acoustic data (which will be explained shortly), so as of now inter-DOM calibration is done entirely on shore.

Finally, we consider the part that is within the scope of this research: i.e. determining the time offset and position of each DU. For both purposes, KM3NeT has robust methods that are able to deliver the final accuracy we need. For positioning, a system of acoustic receivers and emitters is deployed. The receivers are located on the seabed surrounding the detector footprint, whereas the receivers are mounted on the individual DOMs. To accurately monitor the location of the DOMs, the sway of strings due to varying sea currents must be taken into account. Therefore, KM3NeT makes use of 'dynamic position calibration', where the emitters send a repeated signal every 10 minutes to measure position [17]. For the inter-DU time calibration, a 'track quality' approach is implemented. For a set of detector parameters, e.g. the DU (time and position) offsets, a muon trajectory is reconstructed and compared to the measurements. Agreement between the hits produced by the hypothesised track and measured hits is quantified using likelihood L, which is maximised by the set of parameters that correspond to the 'best fit' [18]. An example of determining the time offset of a single DU can be seen in Figure 1.3. Here, the likelihood L can be

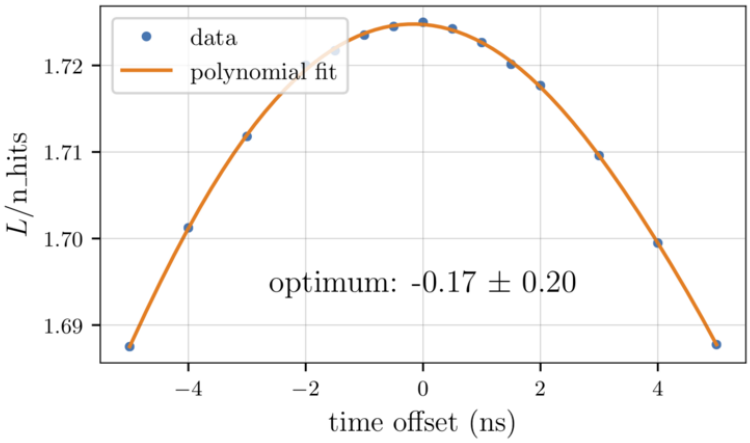

Figure 1.3: *The average track likelihood in the events divided by the number of hits as a function of assumed string time offset. Adapted from* `https://wiki.km3net.de/index.php/Physics_of_muon_calibration`.

approached using a polynomial, which finds its maximum at -0.17 ± 0.20 ns. The results are interpreted as follows: the detector geometry, where this DU has an offset of -0.17 ± 0.20 ns, is most likely to have produced the measured hits.

At this point, finding other methods to achieve the final science sounds like reinventing the wheel. The calibration of both time and position can be performed with the required accuracy and robustness, why bother spending time on developing alternatives? The upcoming section will highlight the relevance of the methods applied in this project, which make use of hit correlations produced by atmospheric muons.

1.10 Goal of this study

Important to mention is that this research is not meant to replace existing methods, but to complement them. This section will address how the hit correlation methods aim to improve our current approach.

Starting off with their unique property: the ability to function independently. Although muon reconstruction results in an accurate estimate of the time offsets, an extensive set of parameters has to be known (e.g. offsets in position and time of each DU and the exact distribution of DOMs along the string). This means it requires data from the acoustic method in order to function. Using hit correlations, we can estimate time offsets

without having any knowledge of the actual position of the strings, and provide DU positions even when time miscalibrations between strings are introduced. Furthermore, the current implementation of reconstruction estimates time offsets one-by-one, while a hit correlation technique estimates them simultaneously.

Another advantage is their fast applicability after deployment. Needing 2-3 days of optical data, these methods are able to estimate the time offsets and positions within 2.5-3 ns and 2 m accuracy, respectively. Although insufficient for the final science, these estimates can be used as a quick initial guess, which can then be refined using the currently used procedures. The methods furthermore require no additional setups or measurements, as they utilise data which would otherwise be regarded as background noise.

Finally, it is important to note that these methods are only in their early stages of development. Throughout this research, we will encounter various flaws in the current approach. To resolve these problems, corners are cut, which results in a significant loss of data and decrease in achievable accuracy. Potential solutions are provided in Chapter 5: when implemented, these methods will be able to perform calibration with higher precision, while requiring shorter periods of data acquisition.

Anyhow, an abundance of available methods cannot be underestimated. A hit correlation approach provides a fast cross check of the results produced by complementary methods, while working completely independently.

The hit correlation methods comprise two components: one that evaluates the individual time offset of each DU, and another that maps the string positions in the horizontal plane of the detector footprint. A detailed description of both will be provided in Chapters 3 and 4, combined with a presentation and discussion of the key findings made during this study. Prior to these, the SN hit correlation data will be addressed, and how they are exploited to form the foundation of these methods. Chapter 6 ultimately presents a conclusion of this study.

Chapter 2

Data

Both methods exploit a characteristic distributional behaviour of the SN hit correlations measured by the detector, that is directly related to both the horizontal distance and time offsets between DUs. The first part of this chapter presents a brief introduction to the nomenclature used throughout this paper and explains how this characteristic behaviour can be described using one single parameter that can be easily extracted from the data. The last section discusses a feature of the data that the methods are unable to account for. As a result, a part of the data is rendered unfit for further analysis and has to be omitted.

2.1 Correlation graphs

The DOMs on a string are ordered from bottom to top and labeled using a floor number, ranging from 1 (closest to the seabed) to 18. They may also be referred to as DOM1, DOM2, ..., DOM18, or DUA.1, DUA.2,...,DUA.18 when considering DOMs on string A. When the floor numbers of two DOMs on different DUs differ by k, those modules are said to be *k'th neighbours*. Correlation of SN hits between neighbouring DOMs is characterised using the time difference between detection events, denoted as δt. The vast majority of correlations will be caused by atmospheric muons, as they are able to travel large distances before their energy reaches below the Cherenkov threshold and their flux is several orders of magnitude higher than that of signals caused by neutrino interactions. As muons enter the detector at various angles and energies, over time, a distribution of δt is measured, which is stored in a 1D histogram called a *correlation graph*. Measuring a certain δt is approximately described by a Poisson process.

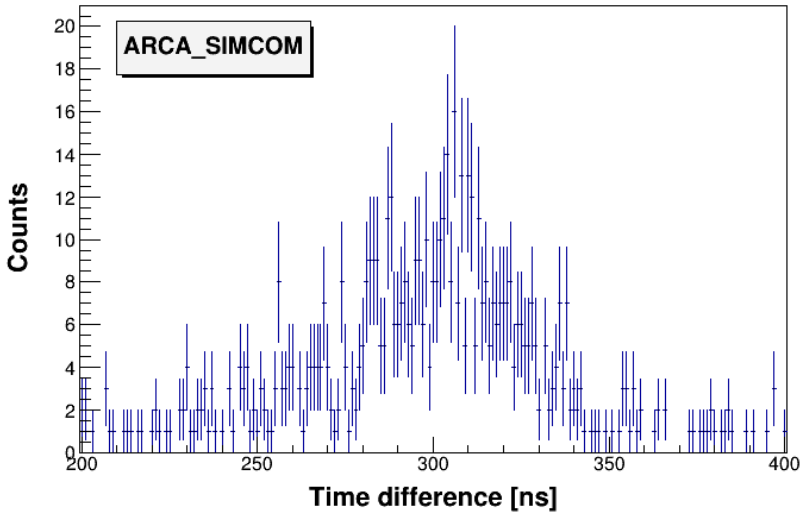

Figure 2.1: *Correlation graph of second neighbours DU24.18 and DU25.16. The error bars reflect the Poisson uncertainties for large samples.*

The error bars in Figure 2.1 are therefore given by the Poisson uncertainty, which is roughly equal to the square root of the number of counts[1]. Subsequently, the correlation graphs of all possible DOM combinations are saved in a 2D histogram format as a ROOT[2] file.

2.2 Real data

The data concern measurements made by the ARCA detector and comprise two components: the before mentioned ROOT file containing the SN hit correlation graphs for a certain combination of runs, and a *detector file* that describes the assumed time and position calibrations of the detector during these runs. In total, 3 different data sets are used, where two of these are merged into a larger set to test the performance of the methods for increasing statistics. The `ARCA_REALMOV` data represent a period with significant swaying (i.e. movement) of strings: this implies an axial tilt measured at the bottom of the string that varies roughly 0.02 radians throughout the runs.

[1]For sufficiently large samples N, the Poissonian distribution of δt converges to a Gaussian with standard deviation $\sqrt{N}$.

[2]Data processing framework created by CERN; visit `https://root.cern/about/` for a detailed documentation.

Table 2.1: *Summary of the real data sets used for this project, measured by the ARCA detector.*

Reference name	Runs	Total length	Date
ARCA_REAL1	13560 13736-13785	$\sim$ 29 h	20 Oct 2022 6-8 Nov 2022
ARCA_REAL2	13399-13409	$\sim$ 33 h	10 Oct 2022
ARCA_REALMOV	13699-13708	$\sim$ 30 h	2-3 Nov 2022
ARCA_REALCOM	13399-13409 13560 13736-13785	$\sim$ 62 h	10 Oct 2022 20 Oct 2022 6-8 Nov 2022

2.3 Simulated Data

In addition to the 'real' data measured by the detector, this research implements Monte Carlo (MC) simulations. These simulations mirror the 3 distinct sets described in Table 2.1, but slightly differ in the acquisition of data. Firstly, only the detection of events (correlation between at least 5 DOMs) is considered, rather than SN hits. As a result, the data contain fewer statistics, which as will turn out, influences the overall performance of the methods to some degree. Secondly, the MC simulations generate hits measured with a static geometry, which implies no string movement. Run 13708 is furthermore excluded from ARCA_SIM3, reducing its total length to $\sim$ 27 h. All simulated sets are again combined to deduce if more data lead to better results.

Table 2.2: *Summary of the Monte Carlo simulated data corresponding to events measured by the ARCA detector.*

Reference name	Runs	Total length	Date
ARCA_SIM1	13560 13736-13785	$\sim$ 29 h	20 Oct 2022 6-8 Nov 2022
ARCA_SIM2	13399-13409	$\sim$ 33 h	10 Oct 2022
ARCA_SIM3	13699-13705	$\sim$ 27 h	2-3 Nov 2022
ARCA_SIMCOM	13399-13409 13560 13699-13705 13736-13785	$\sim$ 89 h	10 Oct 2022 20 Oct 2022 2-3 Nov 2022 6-8 Nov 2022

There is one useful property of the MC simulations that is exploited in this project: contrary to the real data, the exact geometry and time calibrations are known beforehand. The simulated data therefore function as a tool to determine the accuracy of the methods.

2.4 Inter-DU time differences

The goal of this study is to perform calibration on an inter-DU scale. To do so, the sum over all k'th neighbour correlation graphs of string pair A-B is taken to again form a correlation graph that peaks at a time difference Δt_{AB}. For example, the first neighbour DOM combinations would correspond to DUA.1-DUB.2, DUA.2-DUB.3,..., DUA.17-DUA.18. Analogously, the same procedure is applied to conjugate pair B-A (e.g. combinations DUB.1-DUA.2,DUB.2-DUA.3,...,DUB.17-DUA.18 for the first neighbour) to obtain a distribution that peaks at Δt_{BA}.

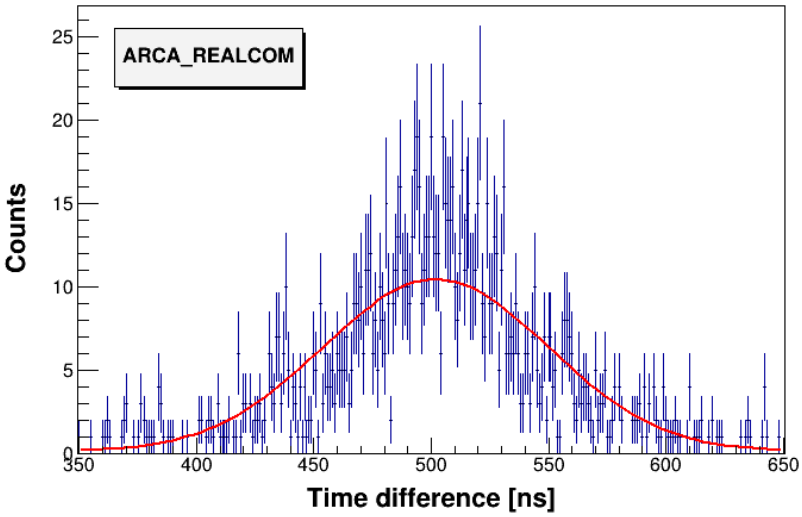

Figure 2.2: *Third neighbour summed distribution of SN hit time differences registered by string pair 14-19 in the ARCA detector. Illustrated in red is a WLS Gaussian fit.*

When sufficient symmetry in the detector geometry is assumed, meaning the strings have perfect vertical alignment and share floors at equal heights (as illustrated in Figure 2.3), the distributions produced by string pairs A-B and B-A should be identical given an isotropic muon

Version of June 30, 2023– Created June 30, 2023 - 14:00

flux. Quantities Δt_{AB} and Δt_{BA} therefore serve as viable characteristic measures for both distributions. Their values can be extracted in a reproducible manner by applying a weighted least squares (WLS) Gaussian fit to the data, and taking the mean parameter as an estimate. This is achieved computationally by making use of the routine `$JPP_DIR/examples/JCalibrate/JOffset_extract`, provided by the JPP software framework[3]. We note that the errors provided to the fit are not a true reflection of the Poisson uncertainty for small counts, as in this regime they should be asymmetric. However, for the purpose of acquiring the parameters of interest, this approach is sufficient.

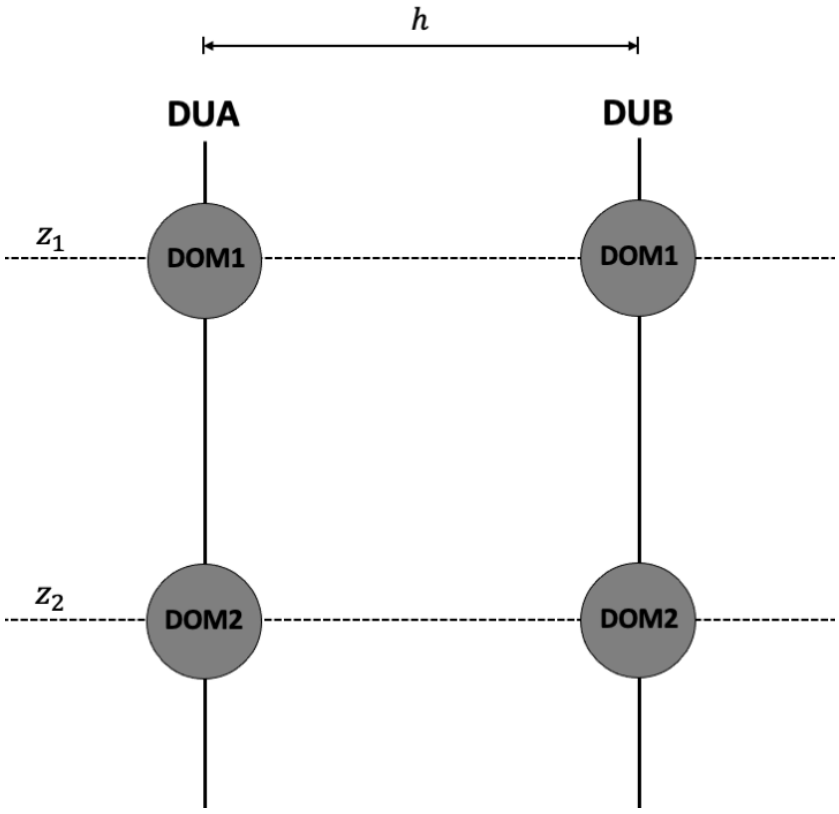

Figure 2.3: *Simplified sketch of the symmetric detector geometry. String A and B have identical floor altitudes z_1 and z_2, and retain a horizontal spacing h throughout their entire length.*

[3]This package contains a large set of C++ interfaces, classes and methods made available to the KM3NeT group [11].

2.5 Data selection

Another important parameter produced by the Gaussian fit is the height of the peak, i.e. the *amplitude*. This quantity will serve as a data quality measure, as low-amplitude correlation graphs correspond to data that would rather be omitted from the evaluations to obtain optimal results. An example is provided in Figure 2.4: the Gaussian fit poorly represents the distribution for low samples, and should thus be excluded from further analysis.

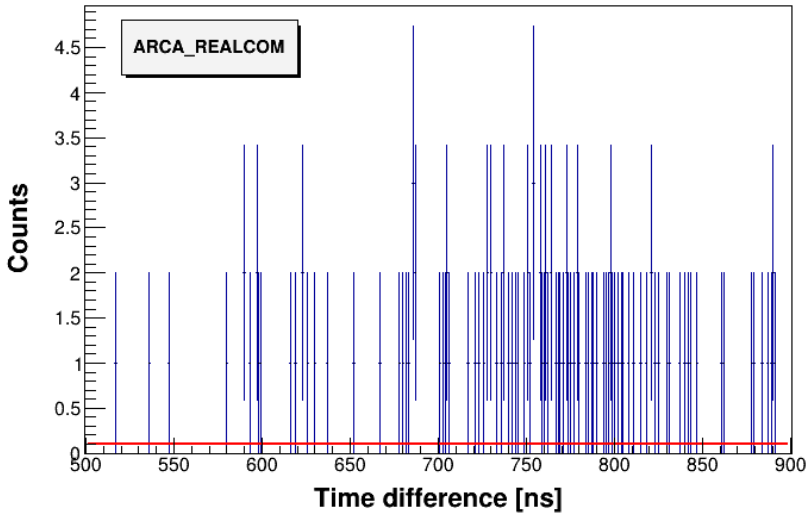

Figure 2.4: *Third neighbour correlation graph of string pair 9-19 in the ARCA detector. The red curve again represents a Gaussian fit on the distribution, which has a small but non-zero amplitude.*

A final selection is imposed on the time differences to filter out 'pathological' data that gravely decrease the performance of the methods. This is achieved by requiring that Δt_{AB} is roughly equal to Δt_{BA}. One selection that has proved to be successful is the *30% cut*:

$$\left| \frac{\Delta t_{AB} - \Delta t_{BA}}{\Delta t_{BA}} \right| < 0.3 \tag{2.1}$$

Which, when combined with an amplitude selection, improves the quality of the data used in further analysis.

Version of June 30, 2023– Created June 30, 2023 - 14:00

2.6 Excluding the first (and second) neighbours

To intuitively understand the results produced by the methods, and explain possible deviations from what is expected, it is always best to question the fundamentals. In our case, this means returning to the inter-DU correlation graphs that are used to extract the time differences Δt_{AB} and Δt_{BA}. During this process, a Gaussian function is fitted over the data to extract the parameter of interest. In most cases, a distribution can be regarded as Gaussian, and using a small exercise one may even show that an arbitrary (possibly asymmetric) density function $f(x)$ with a maximum at $x = 0$ can be approximated with a normal distribution [19]. This approximation fails, however, when a large amount of skewness is introduced. The bell-shaped curve poorly represents the actual form of the distribution, and the estimated mean shifts towards its so called 'fat tail'. As a result, the mean parameter retrieved from the fit inaccurately estimates the true maximum Δt_{AB} of the distribution. For distributions that are roughly normal, such as the one illustrated in Figure 2.5(b), this causes no significant complications. The equal shapes of the distributions of both string pairs A-B and B-A can still roughly be characterised using the Gaussian fit. Hence, the mean parameters suffice to explain any deviation between the two graphs. Performance starts to decrease, however, for heavy-tailed correlation graphs like Figure 2.5(a). In this regime, the fit does such a poor job in describing the distribution that the mean parameter can no longer be used as a characteristic measure.

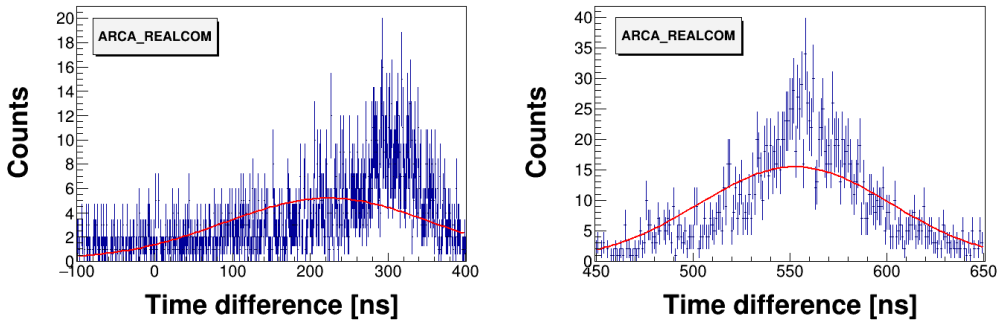

(a) *(b)*

Figure 2.5: *A comparison between the correlation graphs produced by the first (a) and fourth (b) neighbour data of string pair 19-24 ($d_{19-24} \approx 80\,\mathrm{m}$). The red curve depicts the Gaussian fit applied on the distributions.*

Since the negative skewness of the correlation graphs is a natural re-

sult of the angular distribution of muons[4] and geometry of the detector [20], an additional data selection has to be made (aside from the amplitude and 30% cut) that rules out distributions which are considered being 'too skewed'. In the context of this project, this concerns all correlation graphs in which the estimated mean of the Gaussian fit has an offset from the true maximum of the graph that is larger than an expected 5-10 ns. This offset is directly linked to the width of the graph, as a broader distribution implies an increase in the length of the fat tail. As a result, the estimate of Δt_{AB} provided by the fit shifts further away from the true maximum. The width itself is dependent on the neighbour configuration that is considered within a given string combination A-B, as the spread of registered time differences decreases for increasing neighbours k. Consequently, the skewness is most prominent in the lower neighbour regime of each string combination. For the real data, this implies that only the first neighbour fits produce offsets that are substantially larger than the 5-10 ns threshold. The MC simulations, however, are unable to completely reflect the angular and energy distribution of muons, causing a slightly larger spread of data with a heavier left tail. As a result, the second neighbour evaluation has to be excluded in order to optimise results. For higher neighbours, the offsets remain roughly equal, which makes the data suitable for further analysis. From now on, 'all neighbours' refers to neighbours 2-8 and 3-8 for the real and simulated data, respectively, unless otherwise stated.

Omission of the first and second neighbour data is clearly a repercussion of the inability to accurately estimate the distribution of time differences. The assumption of a bell-shaped correlation graph is incorrect, and only approximately valid in the higher neighbour regime. Both methods would, therefore, benefit from implementing a fit that accounts for skewing. A possible solution that can be applied in future iterations of the methods will be discussed in Section 5.1.

[4] That is, the zenith angle θ dependence of the incoming muon flux.

Chapter 3

Time offset evaluation

The time offset evaluation utilises the notion that for a given string pair in the detector, each neighbour configuration measures a correlation graph that is identical to what its conjugate neighbour measures. Miscalibration of the strings therefore manifests itself as a horizontal shift between the correlation graphs produced by equal neighbours. The time offsets can subsequently be extracted from the data by implementing a least squares approach that utilises this shift. Using simplified sketches of the detector, systematics resulting from asymmetries in the geometry can be quantified. The analysis of the data consists of three steps. A valid amplitude cut and an additional data reduction have to be considered in order to produce accurate results. Once this has been established, the evaluated time offsets are used to test the robustness of this method. Finally, a correlation is found between the systematic error and uppermost DOM altitude. By correcting for this correlation, a rough estimate can be provided of the accuracy that is currently obtainable by the method.

3.1 Methodology

Time differences Δt_{AB} and Δt_{BA} are directly linked to the relative offset between the two strings. Provided inter-DOM offsets are negligible and there is a symmetric detector geometry, a perfectly calibrated system should result in equal distributions for string pair A-B and conjugate B-A, with $\Delta t_{AB} = \Delta t_{BA}$. However, when a time offset between the two strings is introduced, the distributions experience a shift relative to each other. We

denote the average shift, otherwise referred to as the relative offset, as

$$o_{AB} = \frac{\Delta t_{AB} - \Delta t_{BA}}{2} \tag{3.1}$$

which can be converted to the individual offsets of the strings. For example, if string A and B experience an offset of $t_A = 30\,\text{ns}$ and $t_B = -20\,\text{ns}$ respectively, their relative offset is 50 nanoseconds. This is generalised by the following equation:

$$t_A - t_B = o_{AB} \tag{3.2}$$

Expanding to a detector that considers n strings forms a system of $N = \frac{1}{2}n(n-1)+1$ equations[1]:

$$\begin{aligned}
&t_1 = 0 \\
&t_1 - t_2 = o_{1,2} \\
&\dots \\
&t_1 - t_n = o_{1,n} \\
&t_2 - t_3 = o_{2,3} \\
&t_2 - t_4 = o_{2,4} \\
&\dots \\
&t_2 - t_n = o_{2,n} \\
&\dots \\
&t_{n-1} - t_n = o_{n-1,n}
\end{aligned} \tag{3.3}$$

Where all offsets are defined with respect to a reference string, which is implied by setting $t_1 = 0$. This set of equations may be written more neatly by introducing matrix A and vectors $\mathbf{t} = (t_1, t_2, \dots, t_n)^T$ and $\mathbf{o} = (0, o_{1,2}, \dots, o_{n-1,n})^T$:

$$A\mathbf{t} = \mathbf{o} \tag{3.4}$$

Which describes an overdetermined system, as there are more equations than unknowns. In general, this does not have a unique solution. Rather, only a 'best estimate' can be provided. Several methods may be used to obtain the desired result, each having its own measure to quantify the 'goodness' of the fit to the data. The two methods most commonly used to estimate linear models like Equation 3.4 are that of *maximum likelihood* (ML) and *least squares* (LS). Both approaches are equally valid and provide

[1] Corresponding to the amount of string combinations, plus one restriction for the reference DU.

the same solution. In this study, the latter of the two is implemented. Appendix A will provide a more in-depth examination of the LS method. For now, it will suffice to mention that the estimator of $\mathbf{t}$, which we will denote as $\hat{\mathbf{t}}$, is derived to be

$$\hat{\mathbf{t}} = (A^T A)^{-1} A^T \mathbf{o} \tag{3.5}$$

The variance of its component $\hat{t}_i$ is given by the i'th diagonal of the variance-covariance matrix

$$\mathrm{Var}(\hat{\mathbf{t}}) = \sigma^2 (A^T A)^{-1} \tag{3.6}$$

where all components of vector $\mathbf{o}$ are assumed to share a common variance σ^2. A popular choice for an unbiased estimator[2] of σ^2 is

$$s^2 = \frac{\mathbf{e}^T \mathbf{e}}{N - n} = \frac{1}{N - n} \sum_{i=1}^{N} e_i^2 \tag{3.7}$$

in which $\mathbf{e} = \mathbf{o} - A\hat{\mathbf{t}}$ denotes the vector of *residuals* [19]. While running the time offset evaluations, this quantity consistently produces uncertainties that are most likely an overestimation of the true measurement error. Preferably, standard deviation σ is estimated using a degrees of freedom corrected mean absolute error (MAE):

$$\mathrm{MAE} = \frac{1}{N - n} \sum_{i=1}^{N} |e_i| \tag{3.8}$$

Its value has a straightforward interpretation: that is, the average deviation of the results from what is measured, where accuracy improves for increasing ratios between the number of equations and unknowns N/n. To execute this method computationally, the JPP software package is utilised once again, this time by running the script `$JPP_DIR/examples/JCalibrate/JMatrix_sol`.

Note that, so far, no specific neighbour configuration is mentioned to produce the data required for o_{AB}. In the case of ideal geometry, the time offsets evaluated in Equation 3.5 should remain equal regardless of which neighbour combinations are considered. Hence, to test the robustness of this method, the time offset evaluation is run for each neighbour configuration separately, and the results are examined for (dis)agreement. All neighbours may also be used synchronously in this method: this increases the amount of equations in System 3.3 proportional to the amount of neighbours considered. Again, a robust method should be able to reproduce the results evaluated for individual neighbours.

[2] Which implies that its expected value equals the true value of the parameter, i.e. $\mathbb{E}(s^2) = \sigma^2$.

3.2 Systematics

Unavoidably, the geometry of the detector is far from symmetric. Although 36 metres on average, inter-DOM distances differ, and the ocean bottom is uneven. As a result, the DOM heights shift relative to each other. Furthermore, the swaying of strings due to alternating sea currents imposes asymmetry between floors. These effects cause an additional relative shift to be measured, which implies that, in general, the assumption $o_{AB} = t_A - t_B$ does not hold in the experiment. For simple geometries, i.e. small deviations from the symmetric one, this systematic error can be predicted. We sketch two scenarios, presented in Figure 3.1: one where two subsequent DOM floors on a DU experience a respective altitude shift Δz_1 and Δz_2, and another in which curved strings impose a horizontal offset Δx from their vertical axis. In both cases, a (anti)muon propagates downwards through the seawater at an angle ϕ with respect to the zenith, emitting Cherenkov radiation towards the DOMs at equal angles θ_c relative to its trajectory. Since the time of arrival of signals at the shifted DOMs

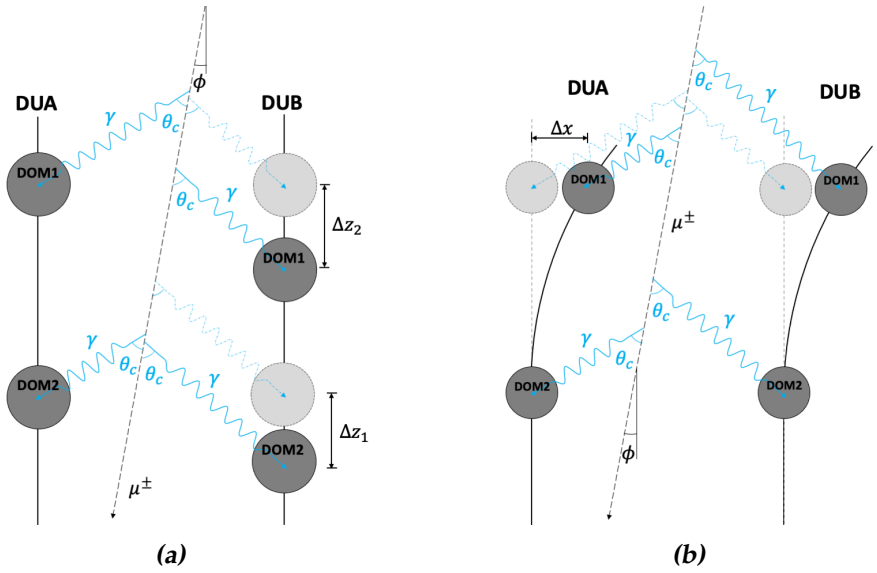

Figure 3.1: *Simplified sketch of hit correlations registered between strings A and B, when either vertical (a) horizontal (b) displacements are introduced to the DOMs. The shaded DOMs and photon (blue; γ) trajectories illustrate a symmetric geometry in which the systematics are not taken into account.*

changes, the relative offset experiences an increase Δo_{AB} linearly propor-

tional to the shifts. In the case of a vertical displacement, this is equal to

$$\begin{aligned}\Delta o_{AB} &= \frac{1}{2}(\Delta z_1 + \Delta z_2)\left(\frac{\sin(\theta_c - \phi)}{v\sin\theta_c} + \frac{\sin\phi}{(c/n)\sin\theta_c}\right) \\ &\propto \frac{1}{2}(\Delta z_1 + \Delta z_2)\end{aligned} \tag{3.9}$$

where v denotes the muon velocity, which is close to c for most muons passing the detector. So even in a perfectly calibrated system, such as the MC simulations, we expect to observe a shift between the correlation graphs of string pair A-B and conjugate B-A that is proportional to some average height difference. Similarly, for the curved string, one derives:

$$\Delta o_{AB} = \cos\phi\left(\frac{1}{(c/n)\sin\theta_c} - \frac{1}{v\tan\theta_c}\right)\Delta x \propto \Delta x \tag{3.10}$$

Note that these equalities not only hold for the first neighbouring DOMs displayed in Figure 3.1, but for general k'th neighbours. As the strings move during the runs, the time difference distribution shifts correspondingly, which makes its peak ill-defined. This leads to a less accurate estimate of Δt_{AB} and ultimately the time offsets. A final asymmetry is imposed by malfunctioning DOMs, which cause 'gaps' in the detector geometry. Even when all previously mentioned systematics are accounted for, these pose a fundamental limit on the accuracy of the method.

3.3 Cutoff amplitude

Introducing an amplitude parameter provides the method with a means to filter inaccurate data. This raises the question of which cutoff amplitude should be chosen to run the evaluation at. When the cut is set too high, the system presented in Equation 3.3 becomes underdetermined due to a lack of correlations. Additionally, we need each string included in the measurements. When setting it too low, poor fits from low sample distributions, such as displayed in Figure 2.4, 'pollute' the evaluation. This implies a range in which the estimates of the time offsets agree, which means the uncertainty does not 'explode'. An example is displayed in Figure 3.2: we note that similar graphs are observed for all strings in the detector. The results in amplitude range 0.2-2.0 vary no more than the estimated uncertainty. As the data in this range are highly correlated[3], the

[3]Note that increasing the amplitude corresponds to selecting a subset of the data at lower amplitudes.

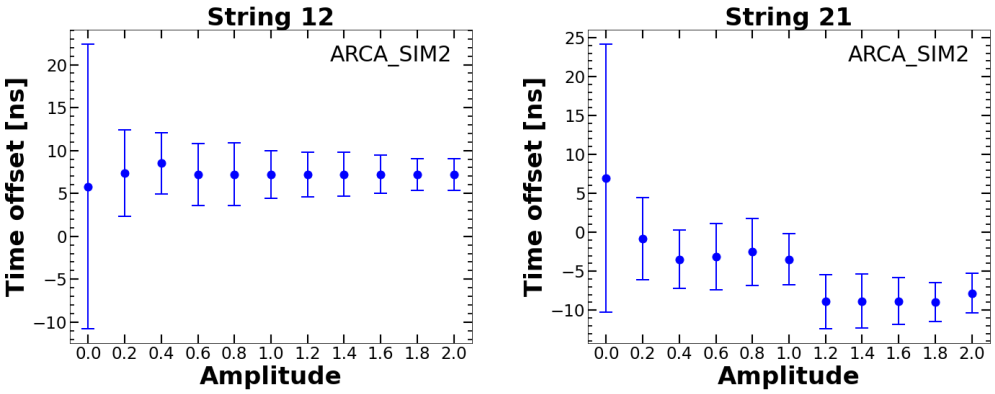

(a) ***(b)***

Figure 3.2: *Offsets of strings 12 (a) and 21 (b) evaluated at several amplitudes for the second neighbour data. For amplitudes greater than 2.0, the evaluation fails due to a lack of statistics.*

method retrieves valid estimates for all cuts chosen in this interval. For individual neighbour evaluation, an amplitude is chosen such that its value is contained within these 'stable regions' of all the data sets.

3.4 Neighbour selection

Aside from the exclusion of the first (and second) neighbour from the analysis, an additional note regarding data set ARCA_REALMOV has to be made. The second neighbour correlation graphs of these runs contain a large fraction of distributions originating from distant ($d_s > 200\,\text{m}$) DU correlations that produce erroneous fits. The amplitude parameters retrieved, however, are sufficiently high to pass the cut. Figure 3.3 presents two of such correlation graphs. Consequently, the second neighbour evaluation pro-

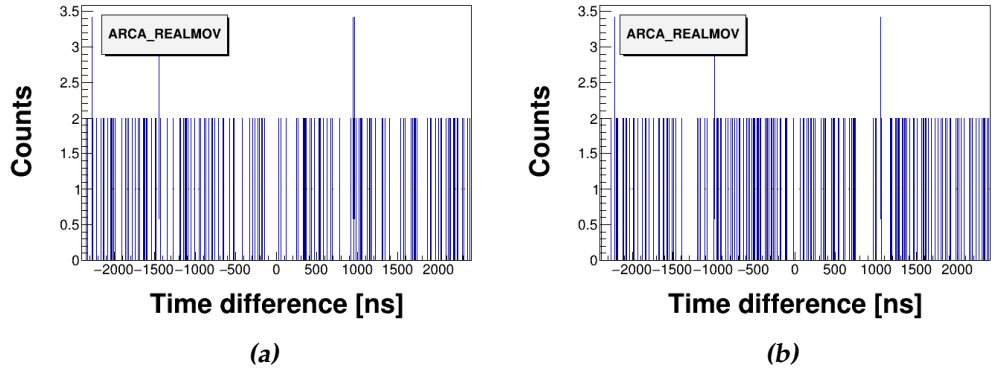

Figure 3.3: *Correlation graphs of string combinations 13-22 (a) and 25-32 (b), with inter-DU distances $d_{13-22} \approx 360\,\text{m}$ and $d_{25-32} \approx 260\,\text{m}$. Both graphs produce erroneous Gaussian fits, that estimate peaks at -2276 and $-2218\,\text{ns}$, respectively, at an amplitude of 2.*

duces unreliable results, with time offsets fluctuating strongly ($\sim 100\,\text{ns}$) between different amplitudes at which the method is run. At amplitudes higher than 2, these fluctuations decrease to roughly 10 ns, with an uncertainty of at least 18 ns. The results in this range, however, cannot be compared with other neighbours, as most evaluations (neighbour 4-8) fail due to a shortfall in statistics. Since the set does produce consistent results for all other neighbours, ARCA_REALMOV is still considered adequate when the second neighbour data is excluded. Similarly, data set ARCA_SIMCOM produces these erroneous fits for the fourth neighbour. We provide two examples in Figure 3.4. The estimated mean parameters, however, are still similar to the true maxima of the correlation graphs. This causes the uncertainty produced by the separate fourth neighbour evaluation to remain somewhat bounded ($< 10\,\text{ns}$). Additionally, these erroneous fits occur in a smaller fraction of the correlation graphs than for the second neighbour of ARCA_REALMOV. The fourth neighbour of ARCA_SIMCOM is hence kept in

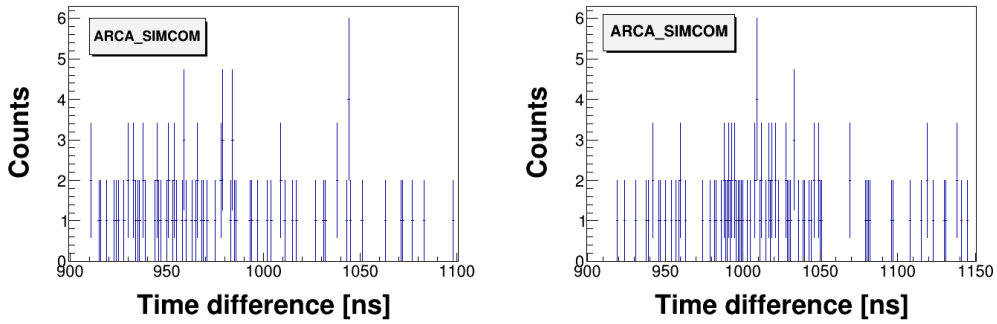

(a) *(b)*

Figure 3.4: *Correlation graphs found for the fourth neighbour of string pair 19-27 (a) and 22-19 (b), with horizontal spacings* $d_{19-27} \approx 250\,\mathrm{m}$ *and* $d_{22-19} \approx 260\,\mathrm{m}$. *The erroneous fits estimate peaks at 1044 and* 1009 ns, *respectively, at high enough amplitudes (>3) to pass the cut.*

the overall evaluation. Data sets `ARCA_SIM1`, `ARCA_SIM2`, and `ARCA_SIM3` contain insufficient data to be analysed at individual neighbour level, and hence can only be used to determine the accuracy of the method once robustness has been established.

The erroneous fits were discovered near the end of this project. In Section 5.2 we will explain their cause, and how they are prevented in future research.

3.5 Results

This section presents an analysis of the evaluated time offsets. We first consider those for individual neighbour configurations to test for consistency of the method. Subsequently, an evaluation is performed on the overall data set. The resulting offsets are examined for linear correlation with two variables obtained from the detector geometry.

3.5.1 Neighbour analysis

Both the simulated and real data are used to test consistency of the results. To examine for agreement between the results of separate neighbours, a chi-square goodness-of-fit test is implemented. The null hypothesis H_0 states that the time offsets estimated for string i are normally distributed around a common value. That is, the weighted mean $\bar{t}_i$ taken over the individual results produced by the neighbours. The weights are chosen to

be $1/\sigma^2_{k,i}$, where $\sigma^2_{k,i}$ denotes the uncertainty of time offset $t_{i,k}$ as estimated by the k'th neighbour. We construct the chi-square statistic for each data set:

$$\chi^2_{\text{DATA}} = \sum_i \sum_k \left(\frac{t_{i,k} - \bar{t}_i}{\sigma_{i,k}} \right)^2 \tag{3.11}$$

Under the assumption of $H_0 : t_{i,k} \sim N(\bar{t}_i, \sigma_{i,k})$, the statistic is $\chi^2(\nu)$ distributed[4]. Quantity ν represents the degrees of freedom, which is equivalent to the amount of evaluated time offsets subtracted by the parameters estimated, i.e. the weighted means. In a data set considering K neighbours and N strings, $\nu = N(K-1)$. The p-value is defined as the probability of obtaining a test statistic χ^2 at least as extreme as χ^2_{DATA}:

$$p = P(\chi^2 \geq \chi^2_{\text{DATA}}) = 1 - F_\chi(\chi^2_{\text{DATA}}; \nu) \tag{3.12}$$

Where $F_\chi(.;\nu)$ is the cumulative distribution function of $\chi(\nu)$. The resulting χ^2_{DATA} statistics and their corresponding p-values are provided in the table below:

Table 3.1: *Chi-square goodness-of-fit test results for the data sets. The second and third column respectively report the applied amplitude cut A and neighbours used for the evaluation.*

ARCA data	A	Neighbours	χ^2_{DATA}	p
`REAL1`	1.0	2-8	80.05	1.00
`REAL2`	1.0	2-8	108.52	0.99
`REALMOV`	0.5	3-8	82.62	1.00
`REALCOM`	1.0	2-8	119.34	0.95
`SIMCOM`	3.0	2-8	130.62	0.37

For all real data sets, the tests indicate a match between the data and null hypothesis, which demonstrates consistency of the method. The lower p-value of `ARCA_SIMCOM` is mostly explained via the third neighbour estimates of string 9 and 13, which are the only data points in the set that deviate more than two $\sigma_{i,k}$ from the weighted mean. The most considerable part of the chi-square statistic originates from string 9, with a contribution of 55.01. Taking a closer look at the time difference data produced by this DU, only 2 correlations are found that have sufficient amplitudes to pass the cut. One of these correlations, string 9 and 10, produces an

[4]Recall, the chi-squared distribution $\chi(\nu)$ describes the sum of squares of ν independent standard normal random variables.

erroneous fit for combination 10-9, returning an estimate for Δt_{10-9} that is roughly 80 ns off from the true maximum of the distribution. Pair 9-10, however, has no trouble fitting and yields a value for Δt_{9-10} that has the expected 5-10 ns offset due to the skewness of the distribution. The computed relative offset o_{9-10} therefore poorly represents the shift between correlation graphs. Since the sample size considers only one additional correlation, namely that of 9 and 13, the OLS estimate of individual time offset t_9 inaccurately represents the actual value. This error propagates and affects the estimate of t_{13}, as for string 13 only 2 correlations are found as well.

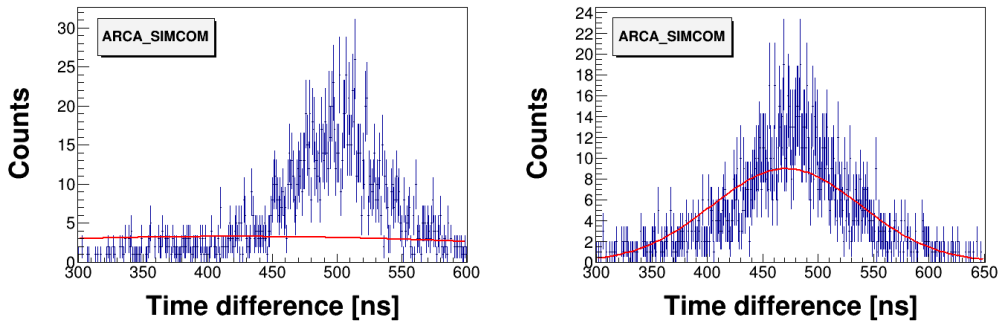

Figure 3.5: *Correlation graph for the third neighbour configuration of string pair 10-9 (a) and conjugate 9-10 (b). The means of the Gaussian fits (red curve) are estimated to be* 418 *and* 471 ns*, respectively.*

The simulated sets evidently suffer from the lack of statistics. Fewer correlation graphs per string are measured, which makes the individual neighbour evaluation more prone to erroneous fits on the correlations that we do measure, such as Figure 3.5(a). For smaller sets like `ARCA_SIM1-3`, the evaluation cannot be run at all. When the neighbours are combined, the sets contain sufficient correlation graphs to accurately estimate the time offsets. For this reason, all MC simulations serve a purpose in the final part of the results.

3.5.2 Linear correlation

The exact geometry and time calibrations of the strings in the simulated data are predetermined, which means individual offsets of strings are set to zero. This is not what the method evaluates in most cases. As mentioned in Section 3.2, a height difference between DOMs causes a shift be-

tween the measured correlation graphs that is linearly proportional, given a symmetric geometry throughout the detector. To establish a linear correlation, the time offsets for each string are evaluated by making use of the combined neighbour data set. Only for ARCA_SIM3, neighbour 4,5 and 7 are omitted as they produce results similar to what is found for the second neighbour of ARCA_REALMOV in Section 3.4. The results are compared against the height of DOM1 and DOM18, which are provided by the detector file. In the ideal symmetry, both of these variables would classify as a measure of the vertical shift between strings. This is achieved in Figure 3.1(a) by imposing identical shifts $\Delta z_1 = \Delta z_2 = \Delta z$ on all floors. As the true detector geometry deviates from this configuration, the question remains whether these 2 variables are able to predict a systematic trend in the time offsets measured for the MC simulations. To infer potential correlation, two WLS linear fits are estimated for each string. Figure 3.6 provides a graphical depiction of the analysis: the graphs of the remaining data sets can be found back in Appendix B.1. The analysis is repeated for the real data sets, in order to determine the systematic effect of swaying strings.

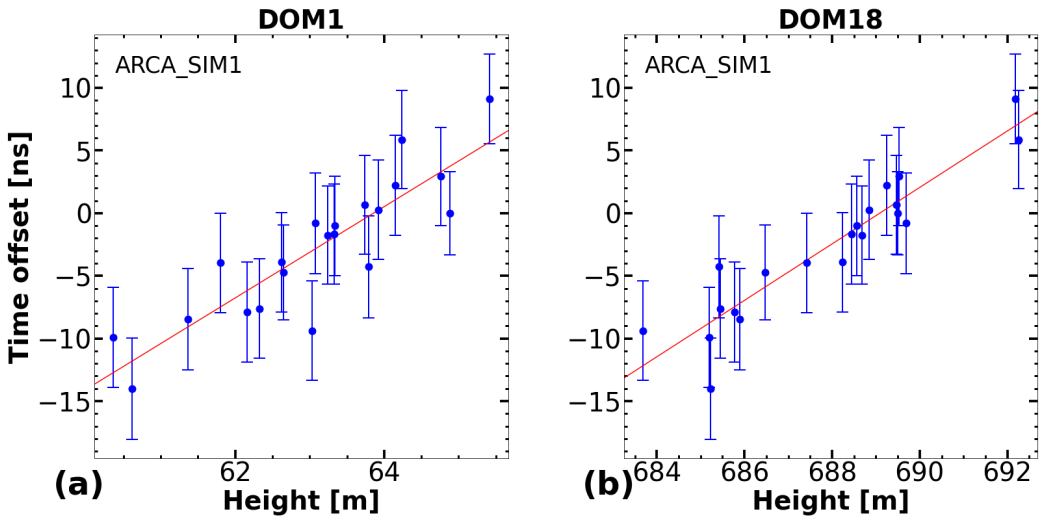

Figure 3.6: *Evaluated time offsets of the combined neighbour set as a function of DOM1 (a) and DOM18 (b) height. The error bars reflect the estimated uncertainties, while the red curve depicts a WLS linear fit applied to the data.*

A chi-square test is again performed to determine how well the fit matches the data. The null hypotheses now states, for the evaluated time

offset t_i of string i with estimated uncertainty σ_i:

$$H_0^j : t_i \sim N(T_i(z_i^j), \sigma_i) \tag{3.13}$$

Index j is used to represent either the DOM1 or DOM18 height, and $T_i(z_i^j)$ denotes the corresponding time offset predicted by the linear fits. The chi-square statistics are constructed for each data set as:

$$\chi_j^2 = \sum_i \left(\frac{T_i(z_i^j) - t_i}{\sigma_i} \right)^2 \tag{3.14}$$

From which the p-values can be computed:

$$p_j = 1 - F_\chi(\chi_j^2; \nu) \tag{3.15}$$

As the linear fit requires two parameters to be estimated, the degrees of freedom are now given by $\nu = N - 2$ for a set of N strings.

Table 3.2: *Chi-square goodness-of-fit test results for each data set. The second and third column respectively report the applied amplitude cut A and neighbours used for the evaluation.*

ARCA data	A	Neighbours	χ^2_{DOM1}	p_{DOM1}	χ^2_{DOM18}	p_{DOM18}
SIM1	1.0	3-8	9.68	0.96	5.18	1.00
SIM2	1.0	3-8	30.77	0.04	7.80	0.99
SIM3	1.0	3,6,8	21.38	0.32	7.70	0.99
SIMCOM	3.0	3-8	33.85	0.02	11.09	0.92
REAL1	1.0	2-8	79.33	0.00	14.94	0.73
REAL2	1.0	2-8	68.41	0.00	14.98	0.72
REALMOV	1.0	3-8	119.32	0.00	56.50	0.00
REALCOM	1.0	2-8	88.95	0.00	18.30	0.50

The test results of the simulated data suggest a linear correlation between the evaluated time offsets and DOM18 altitude, while the DOM1 altitude seems to be unrelated. For sets ARCA_REAL1, ARCA_REAL2 and ARCA_REALCOM, the test still suggests a match between the data and null hypothesis, but with lower confidence. The results of ARCA_REALMOV find no correlation with either of the variables. Systematics imposed by the movement of strings are clearly a significant contributor to the overall error, and dominate for runs with significant movement. Therefore, only for

data that comprise runs with low or no movement, an accuracy of roughly 1 estimated uncertainty can be achieved by correcting for the time offset caused by the difference in DOM18 height. Table 3.3 reports the uncertainties provided by the evaluation. Only those of the simulated data give a measure of accuracy, and are hence included.

Table 3.3: *Summary statistics of the estimated time offset uncertainties σ_i. The last column contains the sample mean of σ_i, taken over the set of strings.*

ARCA data	min (σ_i) [ns]	max (σ_i) [ns]	$\overline{\sigma}$ [ns]
SIM1	3.31	4.07	3.92
SIM2	2.39	2.7	2.63
SIM3	2.36	3.13	2.95
SIMCOM	2.24	2.57	2.51

So why do we only observe a correlation with DOM18 height? Let us return to Equation 3.9, and note that the detector mostly deals with highly relativistic ($v \sim c$) muons for which the Cherenkov angle θ_c is close to 90 degrees. The expression simplifies to:

$$\Delta o_{AB} \approx \frac{1}{2}(\Delta z_1 + \Delta z_2) \cdot \frac{1}{c}(\cos\phi + n \sin\phi) \tag{3.16}$$

Assuming a refractive index $n \sim 1.3$ for seawater, this means a unit increase in average displacement $\frac{1}{2}(\Delta z_1 + \Delta z_2)$ causes a relative shift of roughly 3-4 ns. This implies the following: firstly, the relative shift between correlation graphs produced by the k'th neighbours of DUA.18 and DUB.18 is closely related to the height difference $\Delta z_1 \doteq z_A^{\text{DOM18}} - z_B^{\text{DOM18}}$, as it differs at most 1 metre from quantity $\frac{1}{2}(\Delta z_1 + \Delta z_2)$ for virtually all combinations. Secondly, the k'th neighbours of DOMs lower in the strings produce distributions that peak at roughly the same time difference as those of DOM18, as quantity $\frac{1}{2}(\Delta z_1 + \Delta z_2)$ remains approximately equal for all combinations. As DOM18 is the largest contributor to the overall distribution of string pair A-B and conjugate B-A, the peaks of the summed k'th neighbour correlation graphs will approximately coincide with those of DUA.18 and DUB.18. On the contrary, DOM1 contributes substantially less to the summed k'th neighbour distributions, which means the shift between its individual correlation graphs is a poor representative of the actual relative time difference between the DUs.

Chapter 4

Position calibration

The position calibration method utilises a rather unique behaviour of the correlation graphs. We construct a quantity that is nearly unaffected by all sources of time offsets, and is completely dependent on the horizontal distance between strings. Similar to the time offsets evaluation, the string positions are estimated using a least squares approach, this time numerically rather than analytically. Comparing these to the true locations gives a measure of the accuracy of the method. Prior to the analysis, a suitable cutoff amplitude and additional data reduction have to be considered. In the last section of this chapter, the results of both the simulated and real data are analysed to provide a first impression of the accuracy achievable, and how this is affected by sample size and string movement.

4.1 Methodology

We start by defining the average time difference as $\mu_{t,AB} \doteq \Delta t_{AB} + \Delta t_{BA}$. Introducing individual time offsets t_A and t_B increases Δt_{AB} and Δt_{BA} by $t_A - t_B$ and $t_B - t_A$, respectively. Quantity $\mu_{t,AB}$ is therefore independent of real time offsets. It is furthermore virtually impervious to offsets caused by detector asymmetries, as will be demonstrated in Section 4.2. A third order polynomial relationship can be empirically derived between $\mu_{t,AB}$ and the inter-DU horizontal distance for all neighbours. These polynomials give a distinct correlation between the relative positions of the strings and the time differences they measure. We start by defining the horizontal (x, y) (Easting-Northing) plane in the Universal Transverse Mercator (UTM) coordinate system, where the point of reference is taken to be in grid zone N33 at 587 600 m Easting and 4 016 800 m Northing, 3450 me-

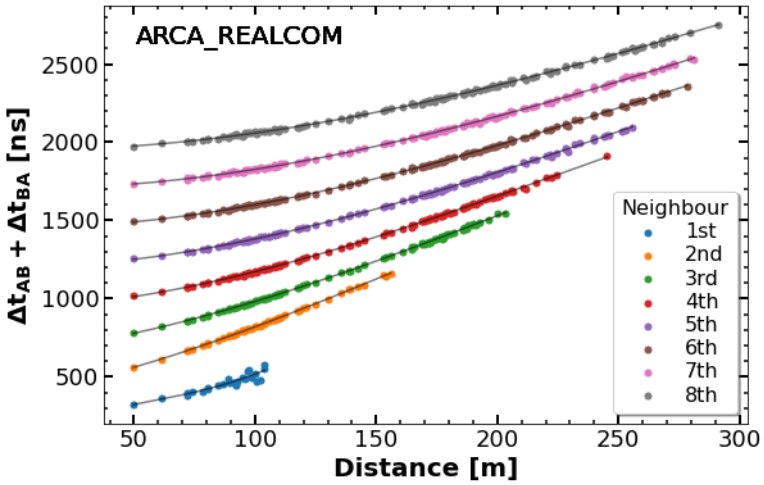

Figure 4.1: *The k'th neighbour average time differences of string pairs in the ARCA detector as a function of their horizontal distance. Fit through the data, to which an amplitude cut of 1 has been applied, are third order polynomials for each individual neighbour.*

tres below sea level. The horizontal positions of the strings are provided by the detector file. They vary slightly between the real and simulated data, mostly with a distance of 10 m, and are assumed constant during all runs. To give an impression of the detector footprint, a graphical depiction of the DU locations is provided in Figure 4.2. Say a new string was to be deployed, and its whereabouts in the (x, y) plane are still unknown or only estimated roughly. As the DU becomes operational right after deployment, time differences with respect to all other strings can already be measured. Assuming all other string locations are known, horizontal distances $d_s(x, y)$ are calculated of all possible string pairs s with the new DU for a given range of potential (x, y) positions. Subsequently, we estimate the average time differences using the polynomials estimated from the data of the remaining strings:

$$M_t(d_s(x, y)) \doteq M_t(d_s) = a_3 d_s^3 + a_2 d_s^2 + a_1 d_s + a_0 \tag{4.1}$$

For each potential location (x, y), an *unweighted* chi-square can be constructed:

$$\chi^2(x, y) = \sum_s (M_t(d_s) - \mu_{t,s})^2 \tag{4.2}$$

Where $\mu_{t,s}$ is the average time difference as measured by the string combinations. Unlike a conventional chi-square, quantity $\chi^2(x, y)$ is not scaled

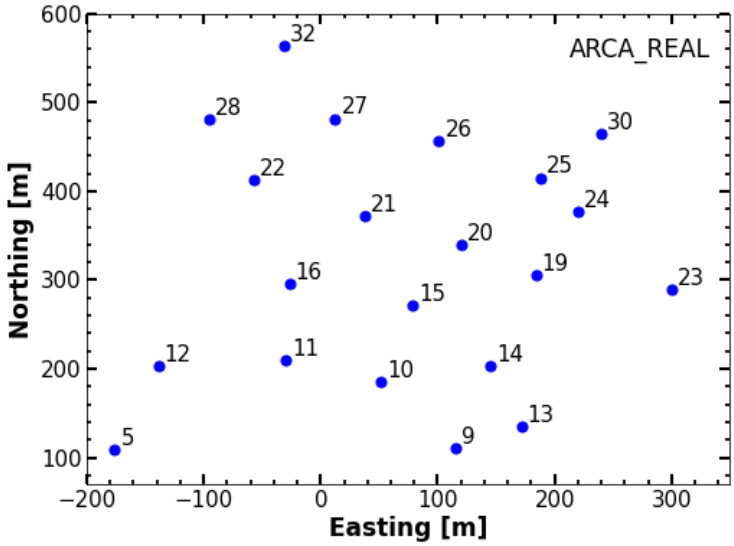

Figure 4.2: *Map of the horizontal string coordinates, relative to the UTM point of reference.*

using a measurement error. Note that this process can be repeated for a given set of neighbours K. The combined chi-square is then given by

$$\chi^2_K(x,y) = \sum_{k\in K}\sum_s (M_{t,k}(d_s) - \mu_{t,k,s})^2 \tag{4.3}$$

with $M_{t,k}(d_s)$ and $\mu_{t,k,s}$ being the estimated and measured average time difference of the k'th neighbour string pair configuration, respectively. The result is a two-dimensional data structure, which is visualised using a heat map in Figure 4.3. We expect the true position of the string, denoted as (x_0, y_0), to minimise the unweighted chi-square. This represents a numerical approach to the LS optimisation:

$$\underset{x,y}{\operatorname{argmin}}\, \chi^2_K(x,y) \tag{4.4}$$

Which produces estimates $(\hat{x}, \hat{y})$ for the location of the new string. The accuracy of the method is quantified by defining a *residual distance*:

$$d_r^{\mathrm{DU}} = \sqrt{(\hat{x} - x_0)^2 + (\hat{y} - y_0)^2} \tag{4.5}$$

Note that this method can be applied to all existing strings in the detector, by assuming their position to be unknown and using the remainder of the

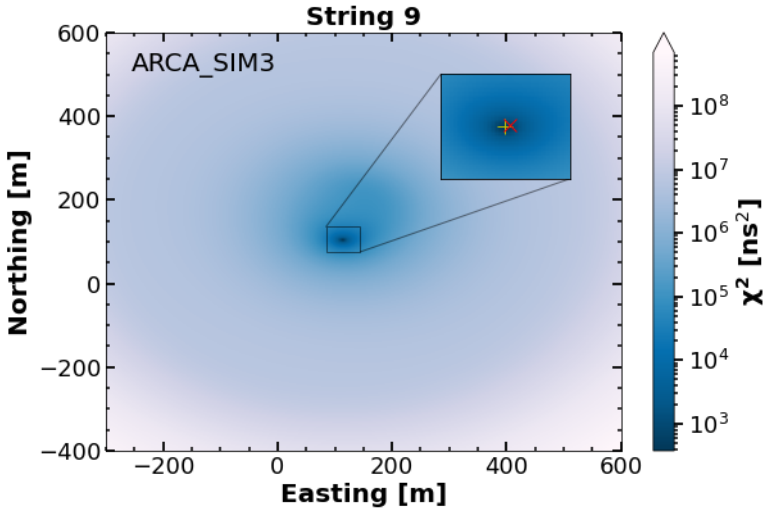

Figure 4.3: *An example of the 2D data produced by evaluating χ^2_K for neighbours 3-8. The true and estimated position of string 9 are indicated with a red cross and yellow plus sign, respectively. Note that χ^2_K has been computed without taking into account the resolution of Δt_{AB} measurements, which grants it units* ns^2*. An amplitude selection of 1 has been imposed on the data to improve accuracy.*

DUs to perform the polynomial fit. It is crucial to distinguish the utility of the real and simulated data in this method. For the real data, only an estimate of the detector geometry is provided by the acoustic method, while the locations of strings are known for simulations. Hence, only the MC data serve as a means to measure the accuracy of the position estimation. To test the performance of this method, both serve a purpose.

4.2 Systematics

For the position calibration, altitude shifts Δz_1 and Δz_2 as displayed in Figure 3.1(a) cause an increase in average time difference $\mu_{t,AB}$ equal to

$$\begin{aligned} \Delta\mu_{t,AB} &= (\Delta z_1 - \Delta z_2)\left(\frac{\sin(\theta_c - \phi)}{v\sin\theta_c} + \frac{\sin\phi}{(c/n)\sin\theta_c}\right) \\ &\propto (\Delta z_1 - \Delta z_2) \end{aligned} \tag{4.6}$$

As quantities Δz_1,Δz_2 are roughly equal for most DOM combinations in the detector, the systematic effect imposed by vertical displacements is negligible compared to the time offset evaluation. For the string move-

ment, this contribution is equal to

$$\Delta\mu_{t,AB} = \frac{2\sin\phi}{v}\Delta x \propto \Delta x \tag{4.7}$$

where Δx denotes the horizontal shift defined in Figure 3.1(b). As the largest fraction of the incoming flux consists of muons propagating downwards ($\phi \sim 0$), the accuracy of the method is again affected to a much smaller degree than that of its counterpart. The average time difference is therefore nearly unaffected by time offsets, whether real or imposed by asymmetry. Even when no offsets are introduced to the geometry of the detector, the accuracy of the method is again limited due to the asymmetry caused by malfunctioning DOMs.

4.3 Cutoff amplitude

Equivalent to the time evaluation, a stable region of cutoff amplitudes has to be established for the method to function properly. In this region, the computed residual distances d_r^{DU} should remain roughly equal, as we are again working with correlated data sets. If the cut is set too low, poorly estimated time differences obtained from small sample distributions, like Figure 2.4, take over. This produces a third order polynomial fit that does not represent the actual relation between average time difference and inter-DU distance.

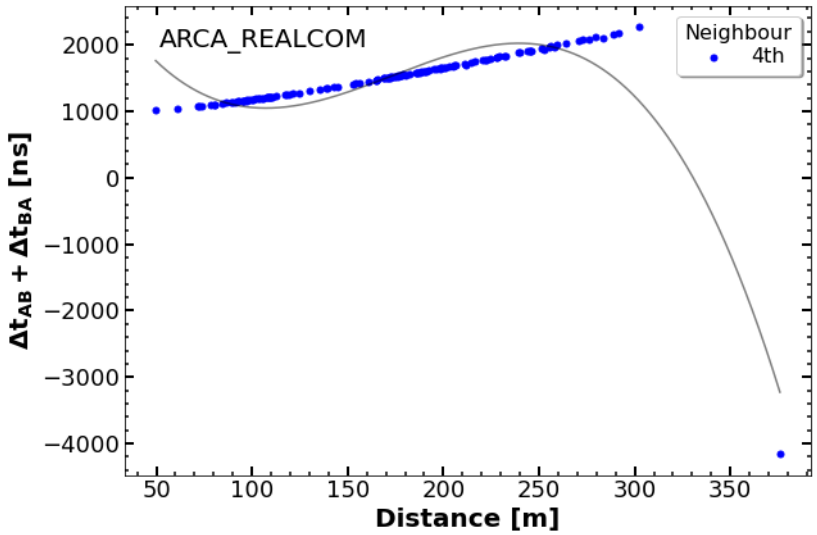

Figure 4.4: *Third order polynomial estimated for the fourth neighbour time difference data and inter-DU distance. The cutoff amplitude is set to 0, which causes an outlier produced by a small sample distribution to interfere with the fit.*

Alternatively, setting the amplitude too high results in a shortage of string correlations. As a result, the unweighted chi-square data has no global minimum. This typically happens first for strings located near the detector boundary, as there are less neighbouring strings in their proximity. An example is shown for DU5 in figure 4.5, which in a 150 m radius only neighbours to DU12. Evaluating its position at high amplitudes produces a ring-like pattern in the heat map of χ^2_K, as it is minimised solely for a certain distance from the true position of string 12.

Version of June 30, 2023– Created June 30, 2023 - 14:00

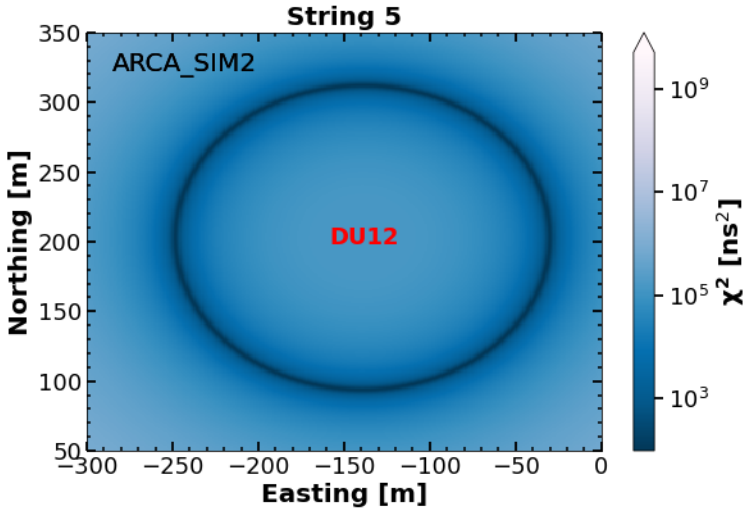

Figure 4.5: *Heat map of χ^2_K, computed for string 5 after applying an amplitude cut of 2 to the time difference data. The exact location of DU12, which follows from the MC simulation, is at* $(-137.980\,\mathrm{m}, 197.710\,\mathrm{m})$.

A time difference may still be measured by several neighbour configurations (in Figure 4.5 these were the 5th and 6th neighbours) of the same string pair, but as these all correspond to roughly the same distance in the third order polynomials, only the band of the ring experiences an increase in size. To accurately perform, the method requires correlation with at least 3 strings, with multiple neighbour configurations involved for each pair. We quantify the spread of residuals and average accuracy of the method by computing the root mean squared error (RMSE):

$$\mathrm{RMSE} = \sqrt{\frac{1}{N}\sum_i \left(d_r^i\right)^2} \tag{4.8}$$

Where the sum is evaluated over a set of N strings. The RMSE is preferred here over the MAE, as it is more sensitive to outliers, which are typically produced by strings at the boundary of the detector (e.g. DU9). A similar reasoning follows as for the time offsets: the amplitude should be chosen, such that the RMSE does not blow up.

4.4 Neighbour selection

The results from Section 2.6, 3.4 and 3.5.2 indicate that a third data selection has to be made in order for the methods to function optimally,

aside from the amplitude and 30% cut. Just like the time offset evaluation, the position calibration requires a more thorough analysis of the separate neighbour data sets to produce accurate results. The first hint is given by data set `ARCA_SIM3`: Section 3.5.2 suggests that neighbour 4, 5 and 7 should rather not be used in the offset evaluation due to pathological fits that have reached a high enough amplitude to pass the cutoff. These inaccurate estimates of Δt_{AB} manifest themselves in an estimated uncertainty that explodes when evaluating the neighbours separately. Likewise, when implementing these data sets in the position calibration, outliers can be seen when plotting the polynomial fits:

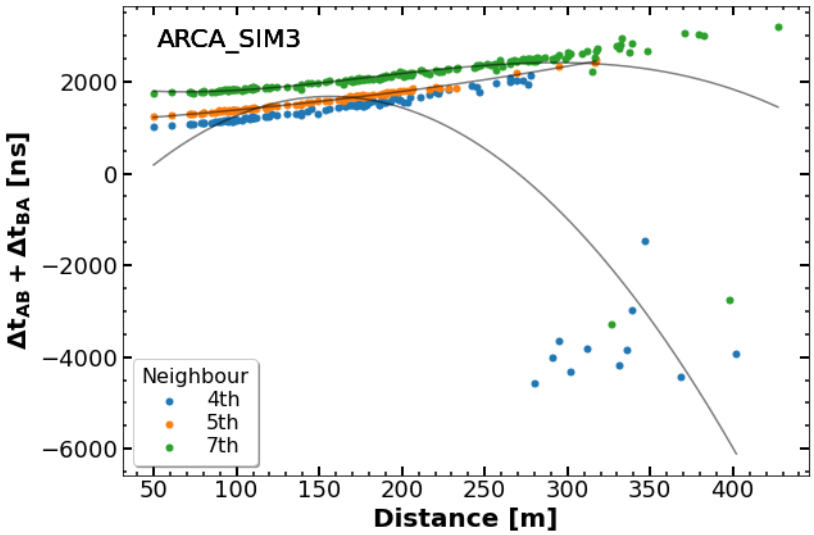

Figure 4.6: *Third order polynomials estimated for the 4th, 5th and 7th neighbour time difference data and inter-DU distance. The cutoff amplitude is set to 0.5, which is insufficient to rule out the outliers.*

Resultantly, the RMSE computed from the residuals blows up. We note that the outliers of the fifth neighbour are small compared to those of the fourth and seventh, but significant enough to decrease the accuracy by nearly a factor 2 when included. By excluding neighbour 4,5 and 7, the outliers disappear and the accuracy of the method improves. In data set `ARCA_SIMCOM`, outliers are found for neighbour seven. The largest one originates from time difference distributions that both have an amplitude of 1. Setting the cutoff this high results in a shortfall in statistics, which means the method does not have a stable region. To resolve this, the seventh neighbour data is excluded from the analysis.

Version of June 30, 2023– Created June 30, 2023 - 14:00

4.5 Results

In the first part of this section, we illustrate the similarities between real and simulated data, to demonstrate that both function as a viable tool to test the performance of the position calibration. Subsequently, the residual distances are analysed to provide a first estimate of the accuracy achievable, and to determine the effects of sample size and moving strings on the predictive power of this method.

4.5.1 Polynomial fits

The real and simulated data produce polynomial fits that are very similar in shape. Only for large inter-DU distances ($d_s > 200\,\text{m}$), deviations start to occur, especially for the third, fourth and fifth neighbour. A plausible cause for this is the inability of the MC simulations to completely reflect the angular and energy distribution of the incoming muon flux, as previously mentioned in Section 2.6. A comparison between fits of data sets `ARCA_REAL1` and `ARCA_SIM1` is displayed in Figure 4.7. The corresponding coefficients are provided in Table 4.1. Overall, the MC simulations prove to be accurate reflections of the real data.

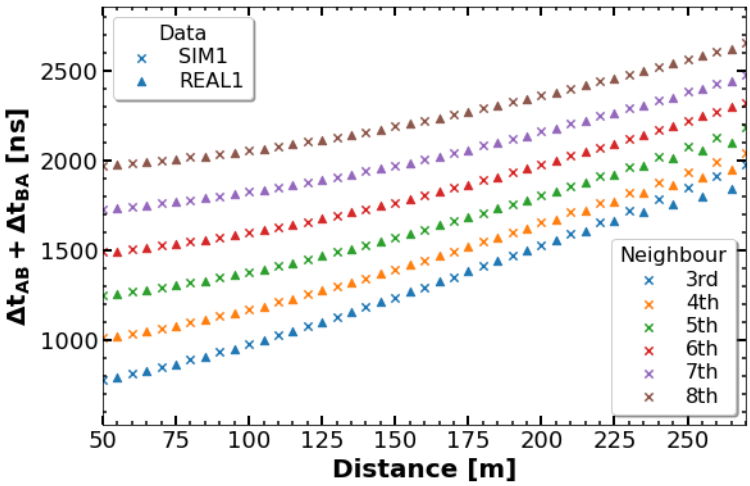

Figure 4.7: *Third order polynomials estimated for real and simulated data. An amplitude cut of 0.5 is applied to both sets to prevent outliers from interfering with the fit.*

Table 4.1: *Estimated coefficients for the third order polynomial fits displayed in Figure 4.7. Quantities a_0,a_1,a_2 and a_3 are as given by Equation 4.1.*

Data	Neighbour	a_3 [ns/m^3]	a_2 [ns/m^2]	a_1 [ns/m]	a_0 [m]
ARCA_SIM1	3	$-7.17 \cdot 10^{-5}$	$3.64 \cdot 10^{-2}$	-0.38	720
	4	$-5.47 \cdot 10^{-5}$	$3.03 \cdot 10^{-2}$	-0.49	970
	5	$-4.61 \cdot 10^{-5}$	$2.78 \cdot 10^{-2}$	-0.84	1231
	6	$-1.43 \cdot 10^{-5}$	$1.52 \cdot 10^{-2}$	0.23	1439
	7	$-9.33 \cdot 10^{-6}$	$1.20 \cdot 10^{-2}$	0.37	1678
	8	$-1.79 \cdot 10^{-5}$	$1.59 \cdot 10^{-2}$	-0.44	1959
ARCA_REAL1	2	$6.50 \cdot 10^{-7}$	$9.19 \cdot 10^{-3}$	3.81	345
	3	$-1.85 \cdot 10^{-5}$	$1.56 \cdot 10^{-2}$	2.09	635
	4	$-3.26 \cdot 10^{-5}$	$2.27 \cdot 10^{-2}$	0.32	946
	5	$-1.79 \cdot 10^{-5}$	$1.70 \cdot 10^{-2}$	0.43	1187
	6	$-2.02 \cdot 10^{-5}$	$1.79 \cdot 10^{-2}$	-0.17	1458
	7	$-1.52 \cdot 10^{-5}$	$1.51 \cdot 10^{-2}$	$-7.71 \cdot 10^{-2}$	1698
	8	$-1.22 \cdot 10^{-5}$	$1.35 \cdot 10^{-2}$	-0.14	1950

4.5.2 Residuals

The residual analysis serves two purposes. We first estimate the accuracy of the method and how this is affected by the sample size of the data. This can only be achieved using the MC simulations, as for these, the exact positions of the DUs are known. The residual distances computed for the real data do not function as a measure of accuracy, as the detector file provides only rough estimates of the true string positions. Finally, the real data is utilised to convey if the effect of swaying strings on the predictive power of the method is truly negligible. A graphical depiction of all residual distances calculated is provided in Appendix B.2. Insufficient correlations for string 9 and 32 were registered in ARCA_SIM2, causing their estimates to be inaccurate. Results seem to improve for increasing statistics; the differences between SIM3 and SIMCOM, however, are rather small, considering the sample size is roughly 3 times as large for the combined set. It seems that the method is reaching the limit set by malfunctioning DOMs. To test this hypothesis, data sets ARCA_SIM1 and ARCA_SIM3 are merged and evaluated. Analogous to ARCA_SIMCOM, the seventh neighbour is excluded to improve results. The statistics of each evaluation are reported in Table 4.2.

Table 4.2: *Summary statistics of the residual distances computed for each data set. The second and third column respectively report the applied amplitude cut A and neighbours used for the evaluation.*

ARCA data	A	Neighbours	min (d_r^{DU}) [m]	max (d_r^{DU}) [m]	RMSE [m]
SIM1	0.5	3-8	0.21	3.58	1.30
SIM2	0	3-8	0.39	13.77	3.48
SIM3	0.5	3,6,8	0.14	2.61	1.35
SIMCOM	0.5	3,4,5,6,8	0.14	1.83	0.87
SIM1&3	0.5	3,4,5,6,8	0.14	1.83	0.97
REAL1	0.5	2-8	0.16	1.36	0.62
REAL2	0.5	2-8	0.21	1.97	0.89
REALMOV	0.5	3-8	0.12	2.33	0.93
REALCOM	0.5	2-8	0.12	1.22	0.64

Indeed, the additional 33 hours of runs in ARCA_SIMCOM have little to no added benefit; selecting a subset of roughly 2.5 days of data results in equally accurate estimates. We observe something similar for the real data: the residuals of ARCA_REAL1 are nearly as large as for ARCA_REALCOM. Lastly, the data hints at a slight decrease in accuracy as a result of swaying strings. To state this with full certainty, a more extensive analysis should be performed on both moving and non-moving data sets, as differences between ARCA_REALMOV and ARCA_REAL2 are slight, while the latter set covers 3 more hours of runs.

Chapter 5

Future extensions

Throughout this study, various deficiencies in the current method have come to light. The two most prominent are found in the analysis and reduction of the time difference data. The Gaussian fit is unable to completely characterise the heavily skewed correlation graphs, which results in the omission of all first (and second) neighbour data. Implementing only the amplitude and 30% cut still results in pathological data, which in most cases gravely decreases the performance of both methods. The first part of this chapter presents possible solutions to both problems, by opposing a new class of correlation graph fits and third data reduction. In the final section, an extension of the time offset and position calibration method is considered, which implements an uncertainty in the measurement of time difference Δt_{AB}. Ultimately, this allows for a measurement error to be estimated for the evaluated string positions.

5.1 Skew distributions

Skewed distributions have been an active field of study over the past decades, as they occur in several fields of science. Financial assets, for example, are known to exhibit extreme tails, which call for the need of alternative methods to measure risk. The energy loss of relativistic charged particles due to ionisation in a thin film was theoretically described by Landau in 1944 [21], which was achieved by introducing an asymmetric probability density now known as the Landau distribution. Determining an accurate fit for the data can be a cumbersome process, as it is highly dependent on their typically elusive nature. One straightforward approach would be to extent commonly used distributions, such that they can ac-

count for skewing. In 1985, a study published by A. Azzalini proposed a new class of probability density functions, in which the skewness is parametrised using a *shape factor* λ [22]. In his paper, he demonstrated that for any symmetric density function $f(.)$ defined on $\mathbb{R}$ with corresponding cumulative distribution function $F(.)$, a third function may be constructed such that for any real λ

$$2f(x)F(\lambda x) \tag{5.1}$$

is a density function. Note that setting $\lambda = 0$ retrieves the original distribution, which by definition implies no skewing. Additionally, location parameter m and scale parameter[1] s are introduced to make these *skew distributions* applicable to the data. The skew density transforms to:

$$p(x; m, s, \lambda) = \frac{2}{s} f\left(\frac{x-m}{s}\right) F\left(\lambda \frac{x-m}{s}\right) \tag{5.2}$$

Intuitively, the first step to take here would be to extend the normal distribution, and fit this over the correlation graphs using a WLS approach. We repeat this step for the logistic, Cauchy and t distribution. Each of these has practical applications and deserves its own dedicated chapter. This section merely functions as a suggestion for possible extensions of the current method used to estimate time difference Δt_{AB}.

The skew distribution fits display visible improvement, especially for the first and second neighbour. An example is provided in Figure 5.1. For each fit, Δt_{AB} is estimated using the argument of the mode. In the higher neighbour regime, discrepancies between estimates diminish, as was to be expected from previous observations. The skew-Cauchy distribution is found to be the most promising candidate, as it visually produces a better fit than the skew-normal and logistic distributions while requiring as much parameters to estimate using WLS. While the skew-t distribution yields similar results, an additional degrees of freedom parameter n has to be included, which unnecessarily complicates the fitting process. Note that these are just a handful of popular skew distributions: Equation 5.2 functions as a gateway to a whole new set of possible fits for the correlation graphs. Alternatives would be intrinsically skewed densities, such as the Landau or Weibull distribution. One may even define a unique distribution tailored to each graph using spline functions: the possibilities are endless. Statistical methods to determine the best fit include the Kolmogorov-Smirnov test and Akaike Information Criterion (AIC)[2].

[1] These are similar in utility to the mean μ and standard deviation σ of the Gaussian distribution, but in most cases no longer serve as a direct measure of the first and second

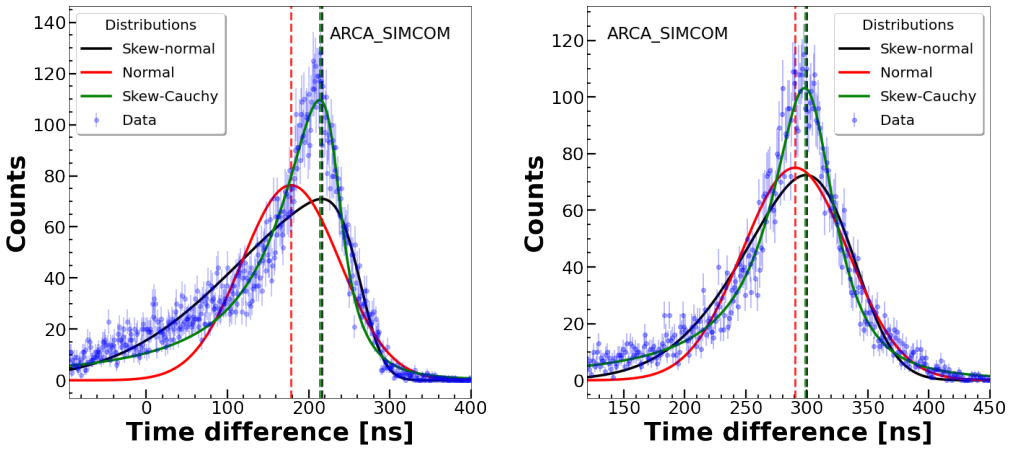

(a) *(b)*

Figure 5.1: *Popular skew distribution WLS fits applied to the first (a) and second (b) neighbour data of string pair 24-25 versus the Gaussian fit (red curve) currently utilised to estimate the time difference Δt_{AB}. The mode of each graph is indicated with a dashed line.*

5.2 Additional selections

It is evident that the amplitude and 30% cut do not filter the data enough to produce accurate results. During this research, a third data reduction is performed which rules out neighbours that contain incorrect measurements of the time difference Δt_{AB}. Both the separate neighbour time offset evaluation and third order polynomial graphs function here as a global quality scan of the data. Note, however, that this procedure also throws out information that could be of use to the method. For example, excluding the seventh neighbour of `ARCA_SIMCOM` results in a less accurate estimation of the time offsets, as only a few outliers occur in the data that mostly influence the position calibration. This brings us to potential extensions that apply to both methods, where techniques are implemented that examine the results for inaccurate estimates of Δt_{AB}. It is found near the very end of this project that a fourth parameter is included in the Gaussian fit, namely a shift in the vertical direction. This shift has negative values for all erroneous fits, such as the ones presented in figures 3.3, 3.4 and 3.5(a).

central moment.

[2]Contrary to the likelihood function, the AIC accounts for the number of parameters estimated.

Excluding it from the WLS fitting process provides two advantages: first of all, the correlation graph in Figure 3.5(a) is now correctly estimated. This will cause a significant improvement in the estimated time offset of string 9 in data set `ARCA_SIMCOM`, implying better chi-square test results for the individual neighbour analysis. Second of all, the fit now produces high uncertainties on the estimates of the mean and width of poorly defined distributions as displayed in Figure 3.3 and 3.4. An additional selection could therefore be based on the relative uncertainty of those parameters, e.g. by imposing the restriction $\sigma_\mu/\mu < 0.01$ for the mean. If one implements a skew distribution fit, an equivalent condition can be set for the scale (s) and location (m) parameter.

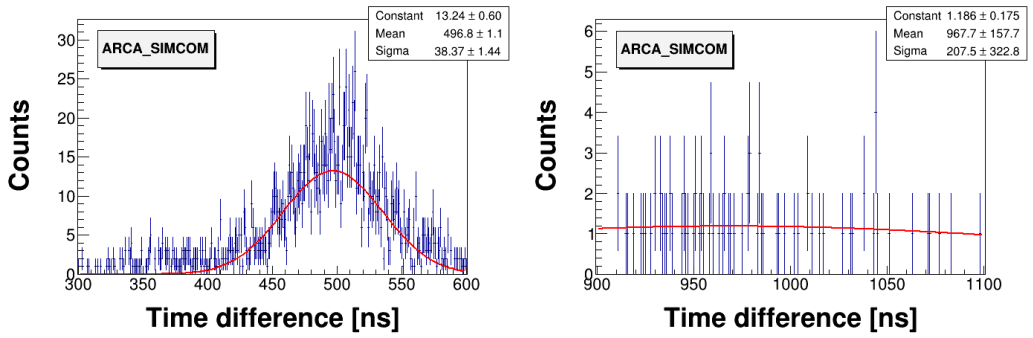

(a) *(b)*

Figure 5.2: *The correlation graph of third neighbour string pair 10-9 (a) shows an improved fit (red curve) compared to Figure 3.5(a), with an estimate of Δt_{10-9} ('Mean' parameter) closer to the true maximum. The fourth neighbour distribution of pair 19-27 (b) has high relative uncertainties on both the mean and width ('Sigma' parameter) estimates.*

5.3 Weighted measurements

Both methods can be extended by including an error in the measurement of time difference Δt_{AB}. For the time offset evaluation, this introduces a weight $w_i = 1/\sigma_i^2$ to each relative offset o_i measured, which alters the mechanics of the LS method. The variance-covariance matrix of the estimated time offsets is now formulated as

$$\mathrm{Var}(\hat{\mathbf{t}}) = (A^T W A)^{-1} \tag{5.3}$$

where W is a diagonal matrix that contains weights w_i. The position estimation is modified in a similar manner, by weighing the chi-square from

Equation 4.3:

$$\chi^2_K = \sum_{k\in K}\sum_{s}\frac{(M_{t,k}(d_s)-\mu_{t,k,s})^2}{\sigma^2_{k,s}+\sigma^2_{k,\bar{s}}} \doteq \sum_{k\in K}\sum_{s}\left(\frac{M_{t,k}(d_s)-\mu_{t,k,s}}{\sigma_{\mu_{k,s}}}\right)^2 \tag{5.4}$$

Where $\sigma_{k,s}$ and $\sigma_{k,\bar{s}}$ are the errors of the time differences estimated for the k'th neighbour of string pair s and its conjugate $\bar{s}$, respectively. A viable measure of $\sigma_{AB,k}$ may be provided by the WLS skew distribution fit proposed in Section 5.1, as the estimated uncertainty of location parameter m. Equivalently, the Gaussian fit provides an error for the mean. Typical values that occurred for the skew-Cauchy fit were around 1 ns, as for the Gaussian fit. This most likely underestimates the actual measurement errors: alternative methods to estimate uncertainty should therefore be considered in future studies. Once an accurate estimate for $\sigma_{\mu_{k,s}}$ is established, χ^2_K is properly normalised. Assuming a sufficiently large set of time differences Δt_{AB} is measured, a confidence region around the minimum $\chi^2_K(\hat{x},\hat{y}) \doteq \chi^2_{K,min}$ can now be defined as the set of coordinates (x,y) such that

$$\chi^2_K(x,y) \leq \chi^2_{K,min} + \Delta\chi^2_K \tag{5.5}$$

where values of $\Delta\chi^2_K$ for 3 popular coverage levels are provided in the table below [15]:

Table 5.1: *Values of $\Delta\chi^2_K$ at frequently used significance levels α.*

1-α (%)	$\Delta\chi^2_K$
68.27	2.30
95.45	6.18
99.73	11.83

Subsequently, an estimate of the error of the evaluated position $(\hat{x},\hat{y})$ can be determined. Important to note is that this region may have several shapes, and in general cannot be regarded as circular[3]. In later iterations of the position calibration method, one may examine for (dis)agreement between results by developing statistical tests that implement the confidence region $\Delta\chi^2_K$.

[3]In this case, a measure of the uncertainty could be the radius of the circle.

Chapter 6

Conclusion

This study presents an examination of two detector calibration methods, capable of evaluating offsets in time and position independently. Both techniques are based on the correlation of Cherenkov photon hits between detection units, caused by the traversal of atmospheric muons through the seawater. They rely on the assumption of symmetries in the detector geometry and use a least square method to provide estimates of the string positions and time offsets.

The time calibration method has already been proven plausible in previous investigations [23]. In this research, we establish a robust method by running the evaluation for several cuts of data (i.e. neighbours), and performing a chi-square goodness-of-fit test to demonstrate consistency of the results. For data sets that consider minor to no string movement, the most prominent source of systematic error is caused by an asymmetry in the detector geometry, which is linearly correlated to the height differences between the uppermost modules of each DU. Ultimately, an accuracy of 2.5 nanoseconds is obtained in this project, which requires roughly 3.5 days of optical data. This requires an additional data reduction, which rules out neighbours that contain inaccurate measurements of the true relative offsets between detection units.

A hit correlation approach to estimate string positions is developed during this project. We show the feasibility of the method by applying it to both measured and Monte Carlo simulated data. The latter of the two is utilised as a means to provide an estimate of the accuracy currently achievable, that is within 2 metres of the true string positions. Further analysis uncovers that 2.5 days of data is sufficient to provide these results. For larger sample sizes, a fundamental limit seems to be imposed on the accuracy of the method by asymmetries in the detector geometry caused

by malfunctioning DOMs.

To reach its scientific goals, KM3NeT requires nanosecond accuracy throughout the detector, which corresponds to a positional accuracy of roughly 20 cm. Although both methods are unlikely to reach these levels of precision, they are only in their early stages of development and are far from reaching their full potential. A hit correlation method furthermore functions as an ideal complementary to the existing calibration techniques, as it implements the background noise from already acquired data. This eliminates the need for additional setups or measurements.

A hit correlation method has been proven feasible for the ARCA detector. Future research can therefore aim to further fine-tune the current techniques used to obtain the time difference data, such that they are able to successfully characterise correlation graphs for lower neighbours. Additionally, the data reduction may be extended to effectively account for pathology. This improves accuracy and preserves valuable data, which ultimately leads to a more efficient method. Another interesting follow-up study would be to apply this method to the ORCA detector, which has a geometry that is much more densely packed with DOMs and has a flatter seafloor than ARCA. Performance of the method is therefore expected to increase, while requiring shorter periods of data acquisition.

Acknowledgements

I would like to express my gratitude towards the KM3NeT group for making this intriguing research project possible, in particular my supervisor Dorothea. You have taught me more about statistics than any course has attempted to do in the past 3 years, and invoked a passion in me for experimental physics that was long thought to not exist. I thank you for your patience and valuable feedback, as without it, this research would not have been possible.

Appendix A

Multiple Linear Regression: Least Squares

Consider a system which contains n linear equations of the form

$$y_i = \beta_1 x_{i1} + \beta_2 x_{i2} + \cdots + \beta_k x_{ik} + u_i \tag{A.1}$$

which in matrix notation can be written as:

$$\mathbf{y} = X\boldsymbol{\beta} + \mathbf{u} \tag{A.2}$$

Vector $\mathbf{y} = (y_1, y_2, \ldots, y_n)^T$ contains n observations on a random variable, also referred to as the *dependent* variable. These are correlated to a set of k *explanatory* variables or *regressors*, used to describe each observation. The result is an $n \times k$ matrix containing nonrandom elements. Possible deviations from the linear model, commonly referred to as the *disturbances* or *errors*, are described within the random $n \times 1$ vector u. The least squares (LS) method aims to estimate the set of parameters $\boldsymbol{\beta} = (\beta_1, \beta_2, \ldots, \beta_k)^T$ such that deviations u_i are as 'small' as possible. This smallness is quantified using the LS *objective function*:

$$S(\boldsymbol{\beta}) = \sum_{i=1}^{n} u_i^2 = (\mathbf{y} - X\boldsymbol{\beta})^T(\mathbf{y} - X\boldsymbol{\beta}) \tag{A.3}$$

Which is simply the sum of squared deviations. Subsequently, it is minimised with respect to vector $\boldsymbol{\beta}$:

$$\underset{\boldsymbol{\beta}}{\operatorname{argmin}}\, S(\boldsymbol{\beta}) \tag{A.4}$$

Applying some vector calculus results in the following solution:

$$\hat{\boldsymbol{\beta}} = (X^T X)^{-1} X^T \mathbf{y} \tag{A.5}$$

Where a hat is used to distinguish the LS *estimator* of $\boldsymbol{\beta}$ from its true value [19]. Some questions that might arise now are: why use the squared deviations to define the 'goodness' of the fit, and e.g. not the absolute value or higher powers? And what is the uncertainty of $\hat{\boldsymbol{\beta}}$? It turns out that the two are related. Namely, in the class of all possible *unbiased* estimators $\tilde{\boldsymbol{\beta}}$ of $\boldsymbol{\beta}$, which means $\mathbb{E}(\tilde{\boldsymbol{\beta}})$ is equal to the true value of $\boldsymbol{\beta}$, we choose the one with the smallest variance. To do so, certain restrictions have to be imposed on this class by making assumptions about the model described in Equation A.2. Aside from linearity in the parameters $\boldsymbol{\beta}$ and nonrandomness of matrix X, we require the observations to have mean $\mathbb{E}(\mathbf{y}) = X\boldsymbol{\beta}$ and common variance $\mathrm{Var}(\mathbf{y}) = \sigma^2 I_n$, where I_n denotes the identity matrix. When these conditions are met, the *Gauss-Markov theorem* states that the best linear unbiased estimator (BLUE) of $\boldsymbol{\beta}$ is the LS solution $\hat{\boldsymbol{\beta}}$. Consequently, its variance is derived to be

$$\mathrm{Var}(\hat{\boldsymbol{\beta}}) = \sigma^2 (X^T X)^{-1} \tag{A.6}$$

which as earlier stated, is the lowest of all linear unbiased estimators of $\boldsymbol{\beta}$. Additionally, if the data is assumed to be drawn from a multivariate normal distribution, i.e. $\mathbf{y} \sim N(X\boldsymbol{\beta}, \sigma^2 I_n)$, we find that the $\hat{\boldsymbol{\beta}}$ provides the best estimate of all unbiased estimators of $\boldsymbol{\beta}$, rather than only those that consist of linear combinations of the data y_i. The last thing to consider is how to estimate variance parameter σ^2. The model has insufficient restrictions to provide one distinct candidate, and only for the class of unbiased *quadratic* estimators one can show that

$$s^2 = \frac{(\mathbf{y} - X\hat{\boldsymbol{\beta}})^T (\mathbf{y} - X\hat{\boldsymbol{\beta}})}{n - k} = \frac{\mathbf{e}^T \mathbf{e}}{n - k} \tag{A.7}$$

has the lowest variance [19]. This leaves open more room for negotiation about how we estimate the actual uncertainty of the data. The *residual* vector $\mathbf{e}$ is used to describe the difference between the observed and estimated values of $\mathbf{y}$, and therefore serves as a measure of accuracy.

Version of June 30, 2023– Created June 30, 2023 - 14:00

Appendix B

Supplementary graphs

This chapter provides graphical representations of the data used to obtain the results in Section 3.5.2 and 4.5.2. We present the remaining time offsets and estimated uncertainties used to obtain the chi-square goodness-of-fit test results as displayed in Table 3.2, and lastly, the residual distances as summarised in Table 4.2.

B.1 Linear fits

B.1.1 Real data

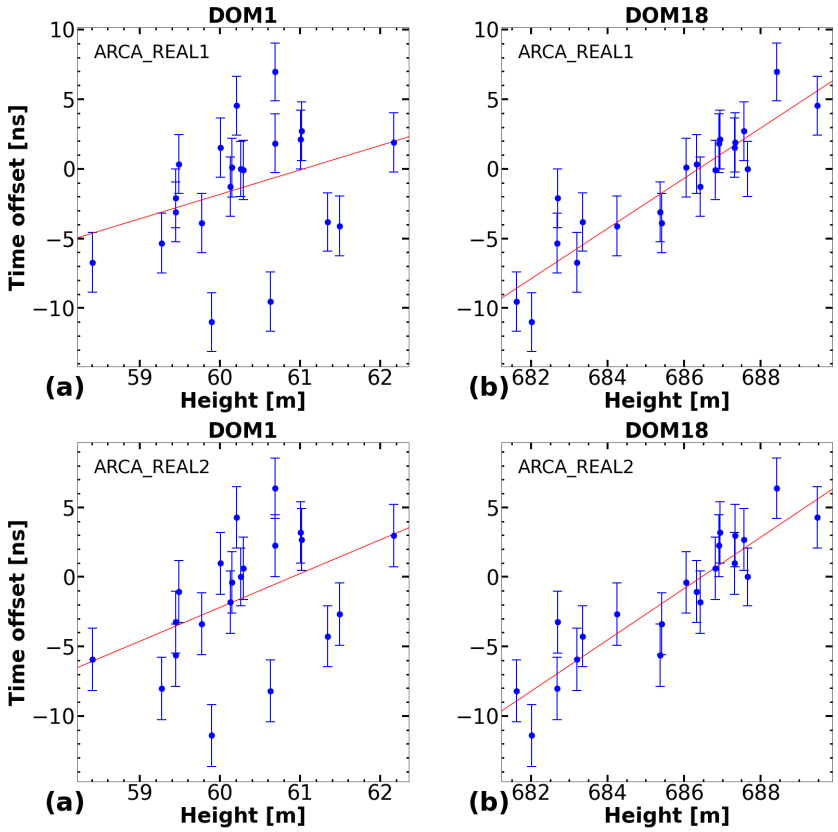

Figure B.1: *Time offsets evaluated for the real data as a function of DOM1 (a) and DOM18 (b) height. The error bars reflect the estimated uncertainties, while the red curve depicts a WLS linear fit applied to the data.*

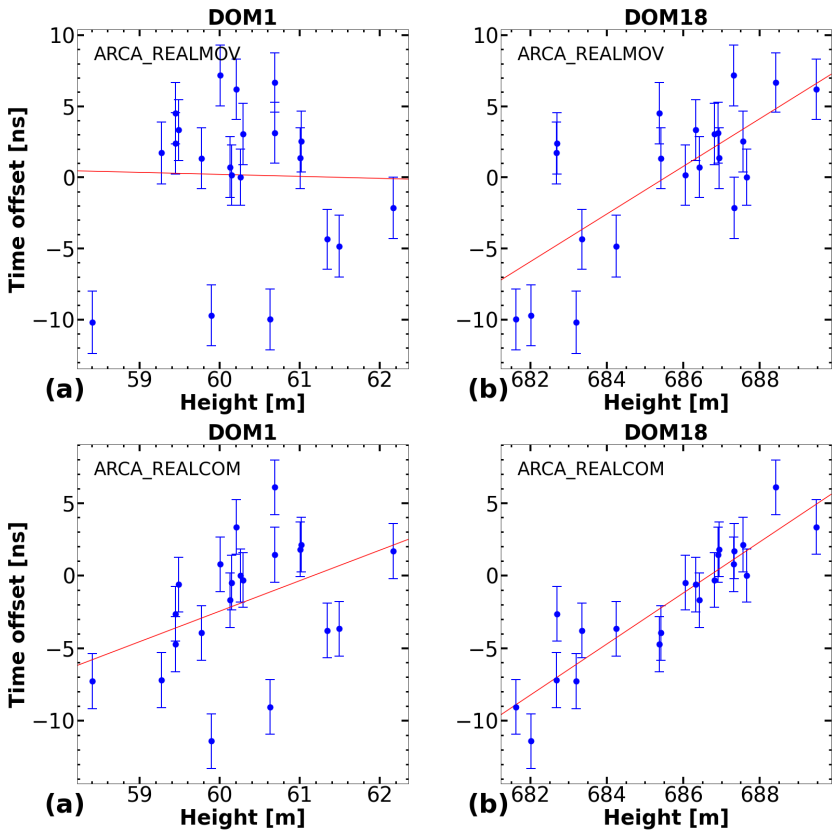

Figure B.2: *Time offsets evaluated for the real data as a function of DOM1 (a) and DOM18 (b) height. The error bars reflect the estimated uncertainties, while the red curve depicts a WLS linear fit applied to the data.*

B.1.2 Simulated data

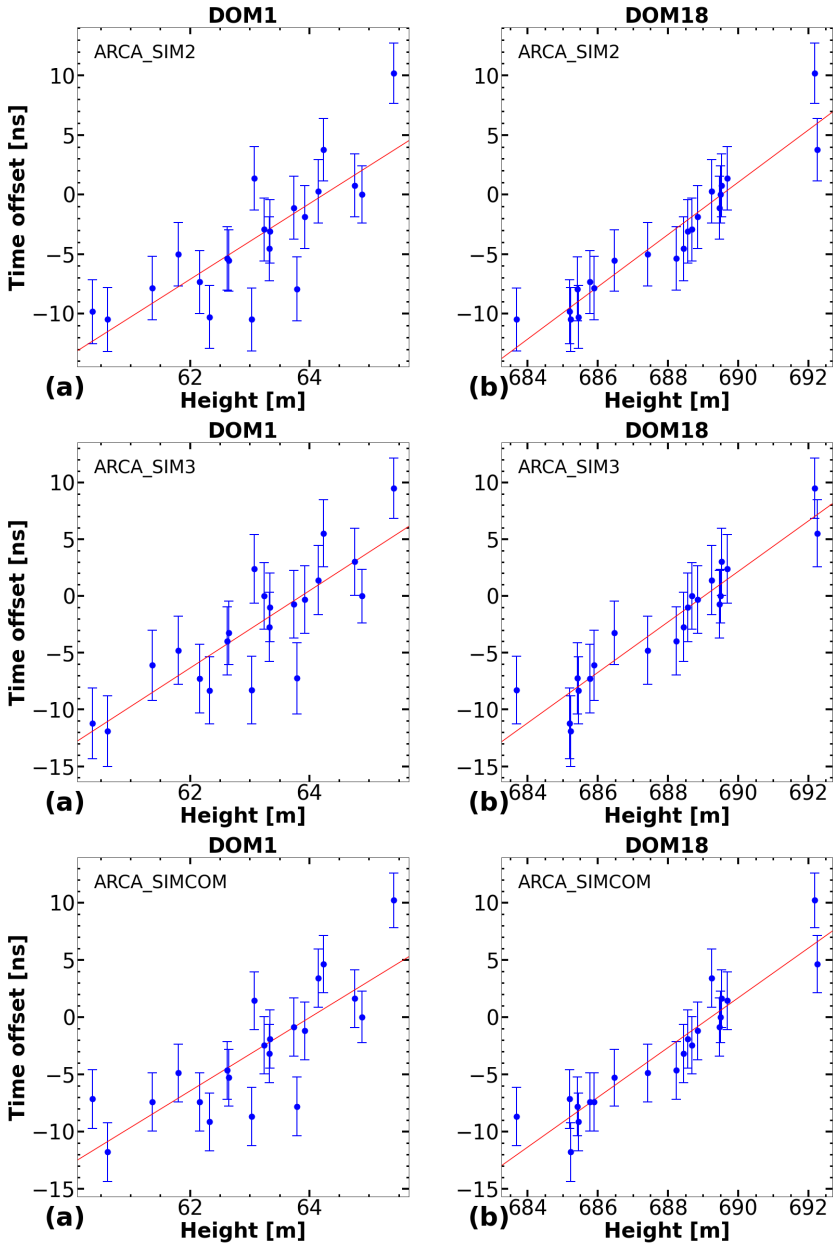

Figure B.3: *Time offsets evaluated for the MC simulations as a function of DOM1 (a) and DOM18 (b) height. The error bars reflect the estimated uncertainties, while the red curve depicts a WLS linear fit applied to the data.*

B.2 Residual plots

B.2.1 Real data

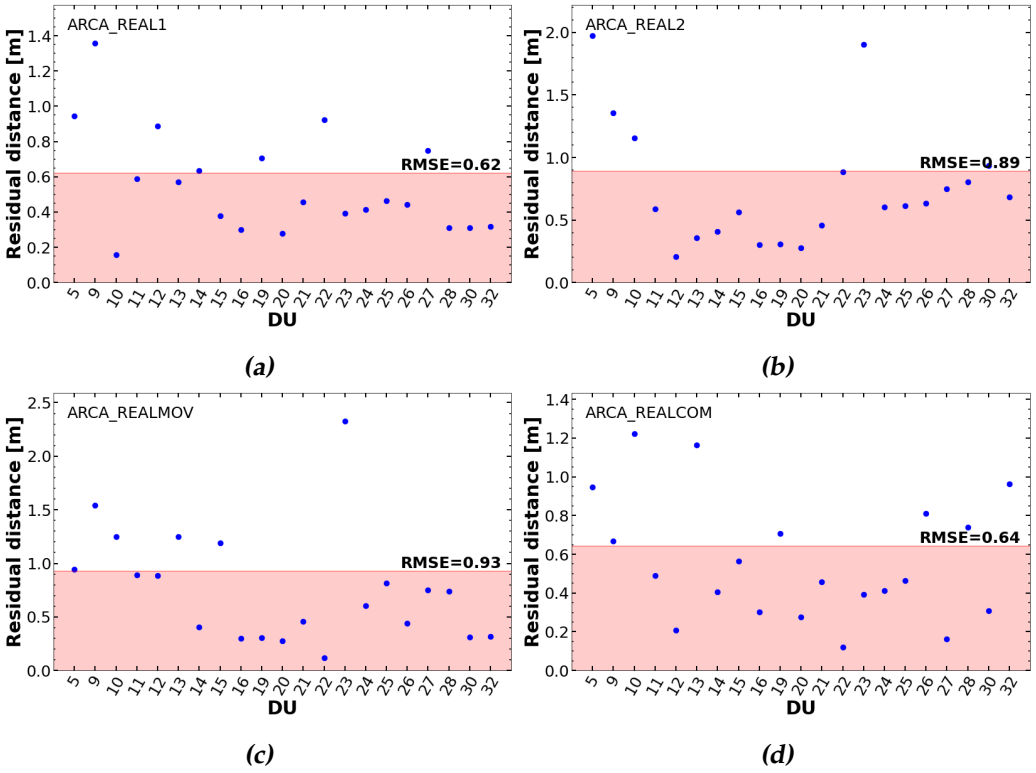

Figure B.4: *Residual distances for the real data sets. The shaded red area depicts the 68% confidence interval spanned by the RMSE.*

B.2.2 Simulated data

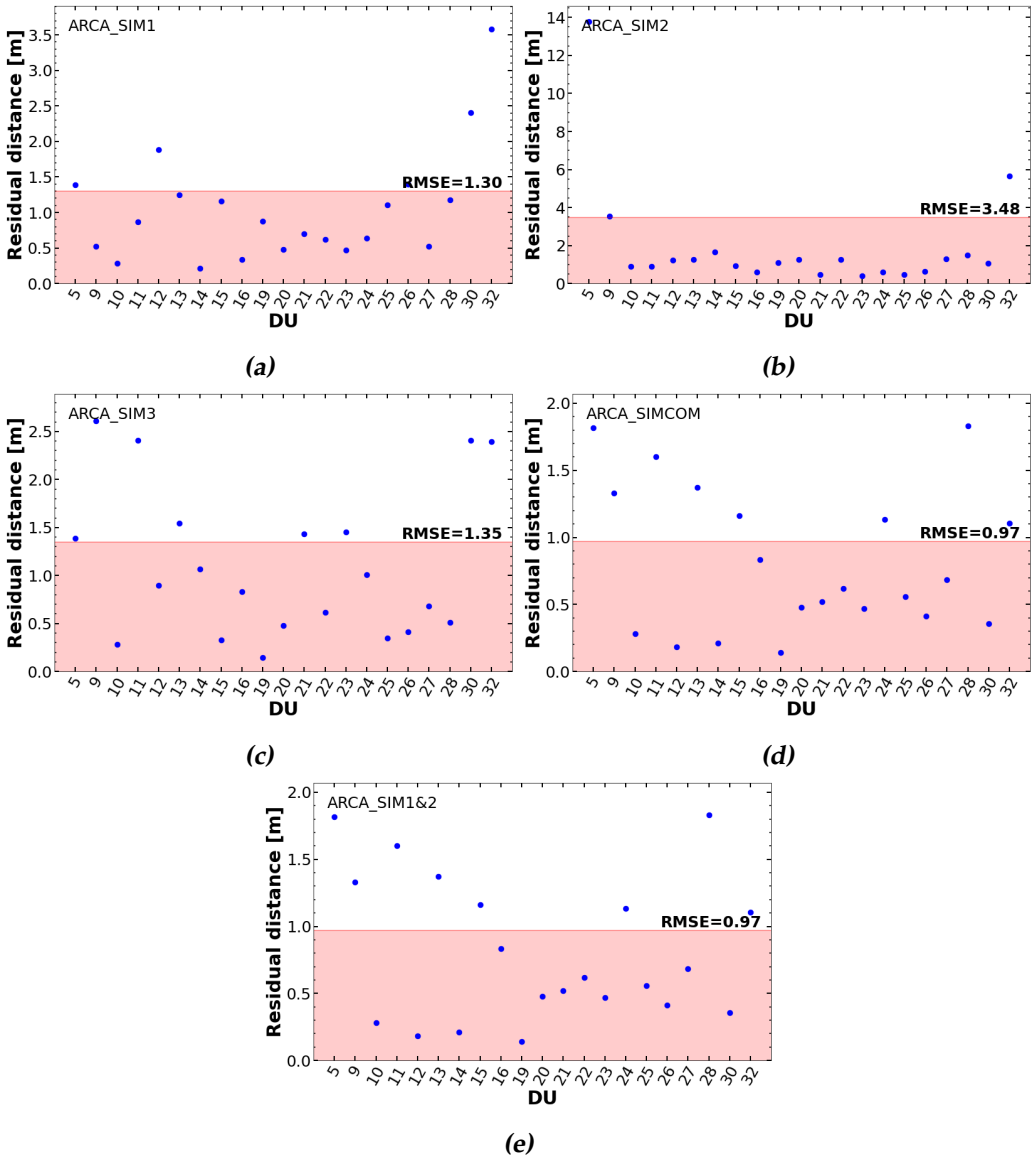

Figure B.5: *Residual distances for the simulated data sets. The shaded red area depicts the 68% confidence interval spanned by the RMSE.*

Bibliography

[1] S Adrián-Martínez et al. "Letter of intent for KM3NeT 2.0". In: *Journal of Physics G: Nuclear and Particle Physics* 43.8 (June 2016), p. 084001. DOI: 10.1088/0954-3899/43/8/084001. URL: https://dx.doi.org/10.1088/0954-3899/43/8/084001.

[2] S Aiello et al. "First observation of the cosmic ray shadow of the Moon and the Sun with KM3NeT/ORCA". In: *The European Physical Journal C* 83.4 (Apr. 2023), p. 344.

[3] IceCube Collaboration*. "Evidence for High-Energy Extraterrestrial Neutrinos at the IceCube Detector". In: *Science* 342.6161 (2013), p. 1242856. DOI: 10.1126/science.1242856. eprint: https://www.science.org/doi/pdf/10.1126/science.1242856. URL: https://www.science.org/doi/abs/10.1126/science.1242856.

[4] IceCube Collaboration* et al. "Evidence for neutrino emission from the nearby active galaxy NGC 1068". In: *Science* 378.6619 (2022), pp. 538–543. DOI: 10.1126/science.abg3395. eprint: https://www.science.org/doi/pdf/10.1126/science.abg3395. URL: https://www.science.org/doi/abs/10.1126/science.abg3395.

[5] A. Zegarelli, S. Celli, and on behalf of ANTARES Collaboration. "Constraining the contribution of Gamma-Ray Bursts to the high-energy diffuse neutrino flux with 10 years of ANTARES data". In: *Journal of Instrumentation* 16.09 (Sept. 2021), p. C09007. DOI: 10.1088/1748-0221/16/09/C09007. URL: https://dx.doi.org/10.1088/1748-0221/16/09/C09007.

[6] S. Aiello et al. "Sensitivity of the KM3NeT/ARCA neutrino telescope to point-like neutrino sources". In: *Astroparticle Physics* 111 (2019), pp. 100–110. ISSN: 0927-6505. DOI: https://doi.org/

10.1016/j.astropartphys.2019.04.002. URL: https://www.sciencedirect.com/science/article/pii/S0927650518302809.

[7] S Aiello et al. "Determining the neutrino mass ordering and oscillation parameters with KM3NeT/ORCA". In: *The European Physical Journal C* 82.1 (Jan. 2022), p. 26.

[8] S Aiello et al. "Combined sensitivity of JUNO and KM3NeT/ORCA to the neutrino mass ordering". In: *Journal of High Energy Physics* 2022.3 (Mar. 2022), p. 55.

[9] S Aiello et al. "Sensitivity to light sterile neutrino mixing parameters with KM3NeT/ORCA". In: *Journal of High Energy Physics* 2021.10 (Oct. 2021), p. 180.

[10] Elena P. Cherenkova. "The discovery of the Cherenkov radiation". In: *Nuclear Instruments and Methods in Physics Research Section A: Accelerators, Spectrometers, Detectors and Associated Equipment* 595.1 (2008). RICH 2007, pp. 8–11. ISSN: 0168-9002. DOI: https://doi.org/10.1016/j.nima.2008.07.006. URL: https://www.sciencedirect.com/science/article/pii/S0168900208009297.

[11] Karel Willem Melis. "Studying the Universe from -3000m N.A.P." PhD thesis. Amsterdam U., 2021.

[12] M Ageron et al. "Dependence of atmospheric muon flux on seawater depth measured with the first KM3NeT detection units". In: *The European Physical Journal C* 80.2 (Feb. 2020), p. 99.

[13] J.D. Haverhoek. "Ultra High Energy Cosmic Ray Extensive Air Shower simulations using CORSIKA". In: (2006).

[14] S. Mollerach and E. Roulet. "Progress in high-energy cosmic ray physics". In: *Progress in Particle and Nuclear Physics* 98 (2018), pp. 85–118. ISSN: 0146-6410. DOI: https://doi.org/10.1016/j.ppnp.2017.10.002. URL: https://www.sciencedirect.com/science/article/pii/S0146641017300881.

[15] R. L. Workman et al. "Review of Particle Physics". In: *PTEP* 2022 (2022), p. 083C01. DOI: 10.1093/ptep/ptac097.

[16] D. Guderian. "Development of detector calibration and graph neural network-based selection and reconstruction algorithms for the measurement of oscillation parameters with KM3NeT/ORCA". PhD thesis. U. Munster, 2022.

[17] Maarten de Jong. *Dynamic position calibration*. May 2023. URL: https://common.pages.km3net.de/jpp/Position_calibration.PDF.

[18] Rosa Coniglione et al. "KM3NeT Time Calibration". In: *PoS* ICRC2019 (2019), p. 868. DOI: 10.22323/1.358.0868.

[19] Jan Magnus. *Introduction to the theory of econometrics*. English. 3rd. 1st edition: 2017, ISBN 9789086597666. VU University Press, May 2021. ISBN: 9789086598519.

[20] S Adrián-Martínez et al. "The prototype detection unit of the KM3NeT detector". In: *The European Physical Journal C* 76.2 (Jan. 2016), p. 54.

[21] Lev Davidovich Landau. "On the energy loss of fast particles by ionization". In: *J. Phys.* 8.4 (1944), pp. 201–205. URL: https://cds.cern.ch/record/216256.

[22] Adelchi Azzalini. "A class of distributions which includes the normal ones". In: *Scandinavian Journal of Statistics* 12 (1985), pp. 171–178.

[23] P. Voerman. "Determination of inter-string time offsets in KM3NeT using Hit Coincidences". Bachelor's Thesis. Leiden U., 2021.